PHYSICAL REVIEW A **87**, 042320 (2013)

Quantum feedback experiments stabilizing Fock states of light in a cavity

B. Peaudecerf,[1] C. Sayrin,[1] X. Zhou,[1] T. Rybarczyk,[1] S. Gleyzes,[1] I. Dotsenko,[1,*] J. M. Raimond,[1] M. Brune,[1] and S. Haroche[1,2]
[1]*Laboratoire Kastler-Brossel, ENS, UPMC-Paris 6, CNRS, 24 rue Lhomond, 75005 Paris, France*
[2]*Collège de France, 11 place Marcelin Berthelot, 75005 Paris, France*

(Received 22 November 2012; published 18 April 2013)

The ubiquitous decoherence phenomenon is responsible for the lack of quantum superpositions at the macroscopic scale. It is increasingly difficult to isolate a quantum system from its environment when its size increases. Making use of the weird quantum properties of mesoscopic quantum states thus requires efficient means to combat decoherence. One option is real-time quantum feedback. It features the components of a conventional feedback: measurement of the system's state (sensor), analysis (controller), and feedback action (actuator) aiming to the target state. The random back-action of the measurements by the sensor makes quantum feedback much more difficult than its classical counterpart. Mesoscopic photon number (Fock) states feature a decoherence rate proportional to the photon number. They are thus a simple example of a fragile quantum resource. We demonstrated recently two quantum feedback schemes continuously stabilizing Fock state of a microwave field in a high-quality cavity. Sensitive atoms, crossing the field one at a time, are used as quantum nondemolition (QND) probes of its photon number. The feedback actuator is either a classical source [Sayrin *et al.*, Nature (London) **477**, 73 (2011)] or individual resonant atoms emitting or absorbing one photon each [Zhou *et al.*, Phys. Rev. Lett. **108**, 243602 (2012)]. Both schemes detect the quantum jumps of the photon number and efficiently correct their adverse effects, preparing and preserving a fragile quantum resource. We present an in-depth analysis of our methods, which sheds light onto the fundamental difficulties encountered in quantum feedback, in particular concerning the state estimation algorithm, and onto the ways to circumvent them. These results open the way to informationally optimal QND measurements or to the stabilization of mesoscopic field state superpositions. More generally, they can be cast in a variety of contexts to loosen the tight constraints set by decoherence in quantum metrology and quantum information processing.

DOI: 10.1103/PhysRevA.87.042320 PACS number(s): 03.67.Pp, 42.50.Pq, 42.50.Dv

I. INTRODUCTION

Feedback control of a complex system, although not always evident, plays a very important role in many domains of our everyday activity. From the simple temperature setting of an oven in our kitchen to the very sophisticated control of a spacecraft docking to the International Space Station, the feedback loop accomplishes basically the same task. It monitors some property of the system to be controlled (e.g., oven's temperature or spacecraft's position), compares it to a preset target value, and, despite all external random perturbations, forces the system to reach the target by correspondingly acting onto it (e.g., by means of the oven's heating resistors or by means of the spacecraft's engines).

The control of *classical* objects is extremely efficient, but the implementation of a simple *measure-analyze-react* feedback loop to a *quantum* system is highly nontrivial. The difficulties are both of technical and fundamental nature. The technical challenge is to measure the quantum properties of fragile quantum systems. This requires both a good isolation of the system from its environment and very sensitive measurement methods. The fundamental challenge comes from one of the most basic postulates of quantum mechanics: any measurement on a quantum system changes its state [1]. The measurement should thus be carefully designed to reduce the perturbation onto the quantum state and its unavoidable back-action should be properly taken into account [2].

The last two decades have witnessed a tremendous breakthrough in isolating and studying individual quantum systems, such as single ions [3], photons [4], etc. The technical challenge on the route towards quantum feedback control has thus been met. This made it possible, for instance, to control with a feedback loop some classical parameters of microscopic systems [5–8].

Several research groups have reported so far on experiments featuring quantum feedback [9–13]. They have achieved the swap of quantum states between qubits [9], the freeze and release of a state evolution [10], an adaptive measurement for a more efficient discrimination between coherent states [11], a qubit's state recovery after spin flip [12], and the control of a driven state evolution [13]. These feedback schemes can be sorted in two main categories. For the autonomous schemes, the controller is embedded into the quantum system [9]. The more flexible active schemes use a measurement, whose result is analyzed by the controller. The optimal control action is then fed back to the system in single shot (the feedback action is triggered only once) [9,10,12] or repeated operation [11,13].

We discuss in this paper two experiments, which have been recently performed in our group [14,15]. In contrast to all experiments cited above, we have realized continuously operated quantum feedback schemes actively stabilizing nonclassical states of a quantum system. The photon-number (Fock) states of microwave radiation stored in a high-Q superconducting cavity are deterministically prepared and then continuously recovered after decoherence-induced quantum jumps. In both schemes, the quantum sensors of the field are circular Rydberg atoms, crossing one at a time the cavity mode in a superposition of two states and interacting with it in the dispersive regime.

---

[*] igor.dotsenko@lkb.ens.fr

The large atom-cavity detuning makes it impossible for the atoms to emit or absorb photons in the mode. However, the atomic frequency is transiently shifted by the field in the cavity, resulting in a phase shift for the atomic state superposition, proportional to the field intensity. A measurement of the atomic state thus provides quantum nondemolition (QND) information on the photon number in the cavity mode [16].

This information is used by the controller, a classical fast real-time computer, to estimate the present cavity state, based upon an extensive knowledge of all experimental parameters and imperfections. This state estimation is used by the controller to decide upon the action of the actuator which will drive the cavity state as close as possible to the target Fock state $|n_t\rangle$ containing n_t photons. Once the target is reached, the controller detects the relaxation-induced quantum jumps, either the loss of a photon into or its creation out of thermal environment, and corrects for them, restoring the target state.

The two experiments use two different types of actuators. In the first [14], we use a coherent classical source to perform small displacements of the cavity field, with an amplitude determined by the controller. This is an experimentally simple procedure. However, this classical actuator, which naturally produces coherent states, is not ideally suited to correct for single-photon quantum jumps. The compensation is thus a rather long process, alternating displacements and QND information acquisition. An efficient stabilization requires that the quantum jump recovery time is much shorter than the lifetime T_c/n_t of the Fock state $|n_t\rangle$, where T_c is the field energy damping time in the cavity. The maximum number of photons in the target state is thus limited to four in this experiment.

In the second experiment [15], we have opted for a fully quantum actuator instead of a classical source. We use resonant atoms to react on the cavity field. Prepared in the upper state $|e\rangle$ of the transition, they can emit a single photon in the cavity. Prepared in the lower state $|g\rangle$, they can absorb a photon. In principle, a single atom is sufficient to compensate for a relaxation-induced quantum jump. The feedback mechanism is thus simpler in its principle and more reactive. It is, however, experimentally more demanding since we must alternate between dispersive atoms, gathering QND information, and resonant actuator atoms. After a careful optimization, we have been able to stabilize photon numbers up to seven.

The aim of this paper is to present in detail all the aspects of these two experiments. We will, in particular, explore the state estimation algorithms, whose performance is essential. They are based on a Bayesian inference for the cavity state, which uses the knowledge of all experimental parameters including imperfections measured in careful calibration experiments, of all measurement results, and of all actuator actions performed so far. We will also present extensive numerical simulations that have been widely used to optimize the experimental parameters and the settings of the feedback mechanism. We discuss the experimental results and the procedures used to assess the efficiency of the feedback.

The paper is organized as follows. Section II is devoted to the general description of the main components of the experimental setup and of the dispersive atom-field interaction. We also describe the main features of the computer control system and give the general structure of an experimental sequence. Section III is devoted to the feedback implementation with a classical coherent actuator. Section IV describes the quantum actuator feedback experiment. We conclude in Sec. V by recalling the main results of the paper and discussing possible extensions of this work.

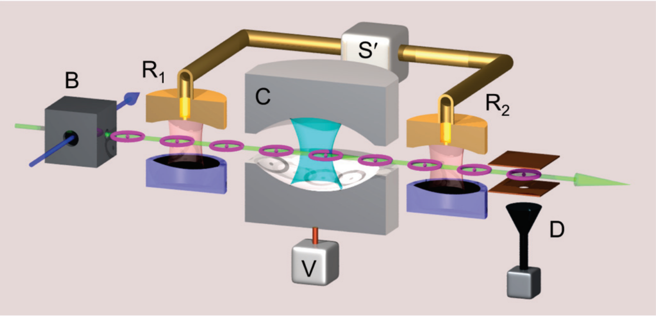

FIG. 1. (Color online) General scheme of the cavity QED experiment. C: high-Q microwave cavity; V: voltage supply to control the electric field in C; R$_1$ and R$_2$: low-Q Ramsey cavities; S′: microwave source. Toroids represent circular Rydberg atoms flying from the excitation zone B towards the ionization detector D.

II. EXPERIMENTAL SETUP AND DISPERSIVE ATOM-FIELD INTERACTION

A. Experimental system

The basic components of our cavity QED setup are depicted in Fig. 1. The microwave field at frequency $\omega_c/2\pi = 51$ GHz is confined in a high-finesse Fabry-Perot resonator C made up of two superconducting niobium mirrors facing each other [17]. The cavity is cooled by a ^{3}He refrigerator down to a temperature of 0.8 K. The field energy damping time reaches $T_c = 65$ ms. At this low temperature, the average number of black-body photons in the cavity mode is only $n_{th} = 0.05$. The mode has a Gaussian transverse profile, with a waist $w_0 = 5.96$ mm, and a longitudinal standing-wave pattern, with nine antinodes separated by $\lambda/2 = 2.94$ mm along the $l = 27.6$ mm separation between the mirrors.

To probe and manipulate the field, we use circular Rydberg atoms, with a large principal quantum number and the maximal value of angular momentum. They are excited in B out of a thermal beam of ground state rubidium atoms. Laser velocity-selective optical pumping and time-of-flight selection determine the atomic velocity $v = 250 \pm 1$ m/s. The low angular momentum Rydberg states directly prepared by laser excitation are transferred into the circular state $|g\rangle$ with principal quantum number 50 by a sequence of radio-frequency and microwave transitions between Stark levels lasting a few tens of μs [18].

The weak laser excitation of the atomic beams results in a Poisson probability distribution for the number m of circular atoms prepared in each sample:

$$P_a(m) = e^{-\overline{m}} \frac{\overline{m}^m}{m!}, \qquad (1)$$

where $\overline{m}$ is the mean number of atoms, typically kept around or below 1.

In order to achieve an efficient feedback, we must send the QND probe samples at the shortest possible time interval $T_a = 82$ μs in all experiments reported here. This time interval is such that each sample leaves the zone B before the next preparation sequence starts.

The QND sensor atoms are cast in a superposition of the levels $|g\rangle$ and $|e\rangle$ (circular state with a principal quantum number 51) in the low-Q cavity R$_1$ by a $\pi/2$ pulse driven by the microwave source S$'$ resonant with the $|g\rangle \rightarrow |e\rangle$ atomic transition at frequency $\omega_{\mathrm{a}} \approx \omega_{\mathrm{c}}$. A second $\pi/2$ pulse is applied in the low-Q cavity R$_2$. It realizes, in combination with R$_1$, a Ramsey interferometer. The atoms are finally detected in g or e by the state-resolving ionization detector D. The ionization is produced by an electric field ramp reaching at different times the ionization thresholds for the two levels. The probability for detecting the atoms in g or e measures the phase shift of the atomic coherence produced by the interaction of the atoms with the field in C.

The atom-field coupling strength in C is measured by the vacuum Rabi frequency $\Omega_0/2\pi = 46$ kHz. The atom-cavity detuning $\delta = \omega_{\mathrm{a}} - \omega_{\mathrm{c}}$, and thus the choice between the resonant ($\delta = 0$) and dispersive ($\delta \gg \Omega_0$) interactions, is controlled by a static electric field produced by a voltage V applied across the cavity mirrors. The resulting quadratic Stark shift of the atomic frequency is -255 kHz/(V/cm)^2.

Note that the lateral extension of the atomic beam ($w_{\mathrm{a}} \approx 1$ mm) is not negligible at the scale of the cavity-mode standing-wave pattern. This leads to a dispersion of the atom-cavity coupling discussed in Secs. II C1 and IV B2.

B. Cavity relaxation

The decoherence of the cavity field results from spontaneous loss or creation of photons to or from the environment. The dynamics of the density operator ρ of the field coupled to an environment at nonzero temperature is described by the master equation [19]

$$\frac{d\rho}{dt} = -\frac{\kappa}{2}(1+n_{\mathrm{th}})(a^\dagger a\rho + \rho a a^\dagger - 2a\rho a^\dagger) - \frac{\kappa}{2}n_{\mathrm{th}}(aa^\dagger\rho + \rho a^\dagger a - 2a^\dagger\rho a), \tag{2}$$

where $\kappa = 1/T_{\mathrm{c}}$ is the cavity decay rate and a ($a^\dagger$) is the photon annihilation (creation) operator. The state evolution during a short-time interval $T_{\mathrm{a}} = \xi T_{\mathrm{c}}$, with $\xi \ll 1$, can thus be approximated by the action of the superoperator $\mathbb{T}$:

$$\mathbb{T}\rho = J_0\rho J_0{}^\dagger + J_\downarrow\rho J_\downarrow{}^\dagger + J_\uparrow\rho J_\uparrow{}^\dagger, \tag{3}$$

where the jump operators J_0, $J_\downarrow$, and $J_\uparrow$ are defined by

$$J_0 = (1 - \xi n_{\mathrm{th}}/2)\, I - \xi(1/2 + n_{\mathrm{th}})\, a^\dagger a, \tag{4}$$

$$J_\downarrow = \sqrt{\xi(1+n_{\mathrm{th}})}\, a, \tag{5}$$

$$J_\uparrow = \sqrt{\xi n_{\mathrm{th}}}\, a^\dagger, \tag{6}$$

with I being the identity operator. They describe events in which the photon number changes by 0, -1, and $+1$, respectively. Note that, in the limit of a zero-temperature environment ($n_{\mathrm{th}} = 0$), we recover, from the expression of $J_\downarrow$, that the lifetime of a photon-number state $|n\rangle$ is equal to $T_n = T_{\mathrm{c}}/n$.

C. Dispersive sensors

1. Ramsey interferometer

The dispersive atom-field interaction results in energy shifts $\Delta E_g(n)$ and $\Delta E_e(n)$ of the atomic states $|g\rangle$ and $|e\rangle$, respectively. These light shifts depend on the field intensity, i.e., on the photon number n. During the atom-cavity interaction, the atomic superposition state $(|g\rangle + |e\rangle)/\sqrt{2}$ prepared in R$_1$ accumulates a phase shift $\varphi(n)$ [4]:

$$\varphi(n) = \int dt[\Delta E_e(n) - \Delta E_g(n)]/\hbar. \tag{7}$$

In the dispersive regime ($\delta \gg \Omega_0$), the energy shifts are proportional to n. Thus, the phase shift also depends linearly upon the photon number:

$$\varphi(n) \approx \phi_0\left(n + \tfrac{1}{2}\right), \tag{8}$$

with the phase shift per photon

$$\phi_0 = \frac{\Omega_0^2 t}{2\delta}, \tag{9}$$

where effective interaction time is $t = \sqrt{\pi/2}(w_0/v)$. The term $\frac{1}{2}$ in (8) accounts for the vacuum Lamb shift. In the experiments reported here, typical values are $\delta/2\pi = 245$ kHz and $\phi_0 = 0.256\pi$, allowing us to discriminate between eight photon-number values [16]. The precise calibration of $\varphi(n)$ and ϕ_0 as well as the experimental verification of the linear approximation (8) are given in Appendix A 1.

The phase shift of the atomic coherence φ, and hence QND information on the photon number n provided by sensor atoms, is measured by the Ramsey interferometer. The final detection of a sensor atom in state $\mu \in \{e,g\}$ modifies the field state according to

$$\mathbb{M}_\mu^{sn}\rho = \frac{M_\mu\rho M_\mu^\dagger}{\mathrm{Tr}(M_\mu\rho M_\mu^\dagger)}, \tag{10}$$

where the superscript sn stands for "sensor." For a sensor initially prepared in state $|g\rangle$, the Kraus operators M_μ associated to this measurement are

$$M_g = \sin\left(\frac{\phi_{\mathrm{r}} + \phi_0(N+1/2)}{2}\right), \quad M_e = \cos\left(\frac{\phi_{\mathrm{r}} + \phi_0(N+1/2)}{2}\right), \tag{11}$$

with $N = a^\dagger a$ the photon-number operator and ϕ_{r} the phase of the interferometer (see below).

Finally, the probability $\pi_g = \mathrm{Tr}(M_g\rho M_g^\dagger)$ to detect the atom in $|g\rangle$ when C contains n photons is a function of ϕ_{r}, ideally oscillating between zero and one, given by

$$\pi_g(\phi_{\mathrm{r}},n) = \tfrac{1}{2} - \tfrac{1}{2}\cos\left(\phi_{\mathrm{r}} + \phi_0(n+1/2)\right). \tag{12}$$

These oscillations, known as Ramsey fringes, result from an interference between two quantum paths for the atom (either transition from $|g\rangle$ to $|e\rangle$ in R$_1$ and then from $|e\rangle$ to $|g\rangle$ in R$_2$, or no transitions at all).

The Ramsey interferometer phase ϕ_r, appearing in the above expressions, is in general the sum of two terms:

$$\phi_\mathrm{r} = \phi_{\mathrm{r}0} + (\overline{\omega_\mathrm{a}} - \omega_\mathrm{r})T_\mathrm{r}. \tag{13}$$

The first one, $\phi_{\mathrm{r}0}$, is the relative phase between the classical resonant pulses in R_1 and R_2. It is constant in all experiments presented in this paper. The second term is the phase accumulated by the atomic coherence with respect to S' during the $T_\mathrm{r} = 360\ \mu$s time of flight from R_1 to R_2 (9-cm separation at 250 m/s velocity). It depends linearly on the source frequency ω_r and on the average atomic frequency for an empty cavity $\overline{\omega_\mathrm{a}}$. The latter can be adjusted by means of a Stark shift resulting from a static potential V_r applied across the mirrors of R_2. In the feedback experiments, the Stark shift is the only parameter used to adjust ϕ_r in real time from one atomic sample to the next. In the calibration measurements, we tune the source frequency ω_r to record Ramsey fringes (see following).

2. *Experimental imperfections*

Our atomic source is nondeterministic with a random number m of atoms per sample. In order to achieve a faithful state estimation, this imperfection has to be included in the measurement operators. Typically, the average number of sensor atoms per sample is $\overline{m}_{sn} = 1.2$. The probability to have more than 2 atoms can be therefore neglected. We thus consider that the probability to have $m = 0$, 1, or 2 atoms is given by the Poisson distribution $P_\mathrm{a}(m)$, truncated after 2 atoms and properly normalized. The set of all possible detection outcomes reduces then to six values $\mu \in \{\varnothing, g, e, gg, ge, ee\}$ ($\varnothing$ stands for detection of zero atoms). They are linked to a new set of Kraus operators, replacing those in (11):

$$\begin{gathered} L_\varnothing = \sqrt{P_\mathrm{a}(0)}I, \quad L_g = \sqrt{P_\mathrm{a}(1)}M_g, \quad L_e = \sqrt{P_\mathrm{a}(1)}M_e, \\ L_{gg} = \sqrt{P_\mathrm{a}(2)}M_g^2, \quad L_{ge} = \sqrt{2\,P_\mathrm{a}(2)}M_gM_e, \\ L_{ee} = \sqrt{P_\mathrm{a}(2)}M_e^2 \end{gathered} \tag{14}$$

with M_g and M_e given by (11). The above expressions of the measurement operators L_{gg}, L_{ge}, and L_{ee} assume that two atoms, simultaneously coupled to the cavity mode, do not influence each other and can be treated independently. We have checked numerically that this assumption is valid in the present dispersive regime. The factor $\sqrt{2}$ in L_{ge} accounts for the indistinguishability of the two atoms simultaneously detected in different states.

The operators M_g and M_e lead to ideal Ramsey fringes (12) with the unity contrast. Figure 2 presents, however, the experimental Ramsey signal, measured as a function of ϕ_r for an empty cavity, with a reduced contrast. It is limited by various experimental imperfections, including the imprecisions on the $\pi/2$ pulses in R_1 and R_2, the stray field inhomogeneities on the atomic beam extension, and the state assignation errors in the detector D. Taking into account all these imperfections, the actual probability $\pi_g(\phi_\mathrm{r}, n)$ can be written as

$$\pi_g(\phi_\mathrm{r}, n) = \pi_o - \frac{c}{2}\cos(\phi_\mathrm{r} + \phi_0(n + 1/2)), \tag{15}$$

where typically $c = 0.79$ and $\pi_o = 0.51$ are the fringe contrast and offset obtained from a sine fit of the signal in Fig. 2.

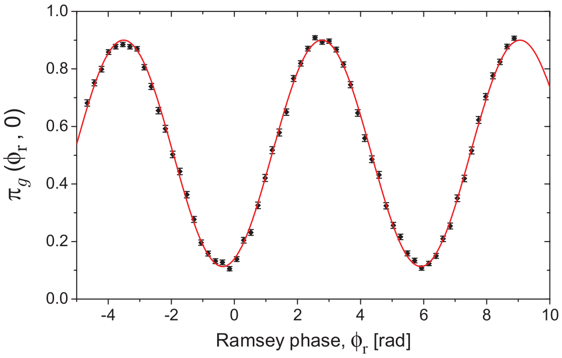

FIG. 2. (Color online) Experimental Ramsey fringes. Probability $\pi_g(\phi_\mathrm{r}, 0)$ for detecting the atom in state g as a function of the Ramsey interferometer phase ϕ_r for an empty cavity. The dots are experimental. The solid line is a sine fit, used to measure the fringe contrast c and offset π_o. In the paper, all presented Ramsey fringes are recorded by scanning the source frequency ω_r while keeping the potential V_r constant.

We have checked theoretically that all Ramsey interferometer imperfections leading to this reduced contrast and finite offset can be modeled as effective state detection errors. They are described by the probabilities η_g and η_e of erroneous detection of state $|g\rangle$ as state $|e\rangle$ and vice versa. These two probabilities are deduced from the Ramsey fringe contrast c and offset π_o following

$$\eta_g = 1 - \pi_o - c/2, \quad \eta_e = \pi_o - c/2. \tag{16}$$

These errors must be calibrated before each experimental run. Their typical values are $\eta_g = 0.10$ and $\eta_e = 0.11$.

Aside from the limited state resolution of the Ramsey interferometer, our detector D has a finite detection efficiency ε (an atom escapes detection with a probability $1 - \varepsilon$). The measurement of ε is described in Appendix A 2. In the present experiments, its value is about 0.3. As a consequence of finite detection efficiency, samples involving different real atom number may lead to the same detection event. This introduces another level of mixing in the expression of the superoperator corresponding to a given detection event.

The field state transformation $\mathbb{M}_\mu^{sn}$ in (10) has been derived for an ideal Ramsey interferometer and a perfect detector. However, because of nonideal detection efficiency ($\varepsilon < 1$) and nonzero effective detection errors ($0 < \eta_g, \eta_e < 1$), one measured outcome μ' corresponds to a mixture of different ideal detection outcomes μ. The conditional probabilities $P(\mu'|\mu)$ are given as a stochastic matrix in Table I. As a result, the estimated state after the measurement (outcome μ') performed on state ρ is given by the action of the superoperator $\mathbb{M}_{\mu'}^{sn}$ defined by

$$\mathbb{M}_{\mu'}^{sn}\rho = \frac{\sum_\mu P(\mu'|\mu)\,\mathbb{L}_\mu^{sn}\rho}{\mathrm{Tr}\big(\sum_\mu P(\mu'|\mu)\,\mathbb{L}_\mu^{sn}\rho\big)}, \tag{17}$$

where we introduce for the sake of simplicity the superoperator $\mathbb{L}_\mu^{sn}\rho \equiv L_\mu \rho L_\mu^\dagger$.

If the sample has not been detected (it is still flying from C to D or has escaped detection in D), the field state transformation

TABLE I. Stochastic matrix showing the probability $P(\mu'|\mu)$ to measure outcome μ' for each ideal measurement outcome μ.

$\mu' \setminus \mu$	$\varnothing$	g	e	gg	ee	ge
$\varnothing$	1	$1-\varepsilon$	$1-\varepsilon$	$(1-\varepsilon)^2$	$(1-\varepsilon)^2$	$(1-\varepsilon)^2$
g	0	$\varepsilon(1-\eta_g)$	$\varepsilon\eta_e$	$2\varepsilon(1-\varepsilon)(1-\eta_g)$	$2\varepsilon(1-\varepsilon)\eta_e$	$\varepsilon(1-\varepsilon)(1-\eta_g+\eta_e)$
e	0	$\varepsilon\eta_g$	$\varepsilon(1-\eta_e)$	$2\varepsilon(1-\varepsilon)\eta_g$	$2\varepsilon(1-\varepsilon)(1-\eta_e)$	$\varepsilon(1-\varepsilon)(1-\eta_e+\eta_g)$
gg	0	0	0	$\varepsilon^2(1-\eta_g)^2$	$\varepsilon^2\eta_e^2$	$\varepsilon^2\eta_e(1-\eta_g)$
ge	0	0	0	$2\varepsilon^2\eta_g(1-\eta_g)$	$2\varepsilon^2\eta_e(1-\eta_e)$	$\varepsilon^2((1-\eta_g)(1-\eta_e)+\eta_g\eta_e)$
ee	0	0	0	$\varepsilon^2\eta_g^2$	$\varepsilon^2(1-\eta_e)^2$	$\varepsilon^2\eta_g(1-\eta_e)$

is given by the superoperator

$$\mathbb{N}^{sn}\rho = \sum_{\mu} \mathbb{L}_{\mu}^{sn}\rho. \tag{18}$$

Note that such an unread measurement does not modify the photon-number distribution $p(n)$, i.e., the diagonal elements ρ_{nn} of ρ. This is a direct consequence of the QND nature of the dispersive atom-field interaction. However, this unread measurement does change the nondiagonal elements of ρ, carrying phase information on the field. The effect of unread measurements must thus be taken into account when the field coherences play an important role. This is clearly the case when we use a coherent source as an actuator.

D. Control system

The timing and management of the feedback experiment is realized by the combination of two computer-control systems running in parallel. The *deterministic* control calculates and executes predetermined sequences of digital and analog outputs realizing all invariable experimental settings and event triggers. For instance, it controls the laser pulses for repetitive Rydberg state excitation, the potential voltage ramps for atomic state detection, the frequencies of all radio-frequency and microwave generators, etc. The *adaptative* control, based on an ADwin Pro-II system (Jäger Messtechnik), acts as the feedback controller K. It performs, in real time, data analysis and sets values of several experimental parameters, thus realizing the feedback action.

The adaptive system includes a CPU board (clock frequency 300 MHz, with a computing power close to 150 Mflops) and a set of digital and analog input-output boards and input gated counters. Its operation in each feedback loop is triggered by an input signal sent by the deterministic system immediately after an atomic sample detection. The first task of the adaptative system is thus to record the number of atoms detected in states $|e\rangle$ and $|g\rangle$.

The main task of the CPU is the state estimation, based on the atomic detection and on all previously available information. This rather complex computation, the principle of which is detailed in the next sections, must be completed in a time shorter than the time interval $T_{\mathrm{a}} = 82$ μs between two atomic samples. The code is thus carefully optimized to minimize computational overheads. All quantities known *a priori* are precalculated. All matrix multiplications are expanded term by term to avoid time-consuming iteration loops. This code is automatically generated by an appropriate precompiler.

Once the state estimation has been performed, the CPU decides upon the actuator settings and programs accordingly the ADwin output channels. The digital output board sets for instance the duration and phase of the coherent field injection (coherent feedback scheme in Sec. III) as well as the duration of the Ramsey pulses in R_1 and R_2 manipulating the atomic states (atomic feedback scheme in Sec. IV). The analog output boards control the Ramsey phase ϕ_{r} by setting the potential V_{r} applied across R_2 (both schemes) and the atom-cavity interaction *via* the electric field in C controlled by V (atomic scheme). At the end of its operation, the CPU enters an idle state and waits for the next trigger from the deterministic control.

All information about state estimation and actuator decisions for the complete feedback sequence is stored in the internal memory of the ADwin system. It is thus possible to check offline the operation of the feedback system and to analyze the decision making of the controller.

E. Basic experimental sequence

A feedback experiment typically consists in 4000 repetitions of an elementary sequence. This sequence itself is divided into three parts. We first prepare an initial field in C: vacuum or coherent state for the feedback with quantum (Sec. IV) or coherent (Sec. III) actuator, respectively. We then operate repeatedly the feedback loop. Finally, we perform an independent reconstruction of the cavity field photon-number distribution, assessing the performance of the system.

In order to prepare the initial state, we have first to get rid of thermal photons and of the field left over by the previous run of the sequence. We thus send through C about 100 resonant atoms prepared in state $|g\rangle$ and tuned at resonance with the mode by a proper setting of the voltage V. They behave as a zero-temperature reservoir and efficiently absorb any photon left in C. Once the vacuum is obtained, we inject the initial coherent state for the coherent feedback (see Sec. III A).

For the feedback operation, we program a long sequence of atomic samples, indexed by the integer k, prepared at time intervals T_{a}. As described in the previous paragraph, the detection of sample k triggers the execution by K of the state estimation and actuator decision in the kth feedback loop. This task is completed in a time shorter than T_{a}.

The situation is slightly complicated by the finite atomic time of flight from C to D, separated by 86 mm. At the time sample k is detected, there are thus $s = 4$ samples which have interacted with C but have not yet been detected by D (see Fig. 1 for a schematic representation of the sample positions at this time). The yet unread detections of these s samples must be taken into account by K in its state estimation. The feedback action calculated after detection of the kth sample is applied shortly before the sample number $(k+s+1)$ enters C.

The end of the feedback operation can be decided upon in two ways, corresponding to two realistic modes of operations for an experiment in which the target Fock state would be used as a quantum resource. In the first operation mode, we require the resource to be ideally ready at all times. In this "steady-state mode," we thus run the feedback for a prescribed arbitrary time interval, typically more than twice the cavity damping time T_c. As will be seen in Secs. III E2 and IV F2, the feedback process reaches, on the average, its steady state long before this time.

In the steady-state mode, the feedback has a chance to be halted during a quantum jump recovery process, when the state is far from the target. This is obviously not the optimal use of a feedback mechanism if one aims on the purity of the target state disregarding the precise preparation time. One generally takes into account information provided by the controller and uses the system only when its state is estimated to be close to the setpoint. We thus implement a "convergence mode" of operation. The feedback is stopped as soon as the fidelity of the target state, i.e., probability to have n_t photons, reaches a predefined threshold (typically 0.8) in three consecutive loops.

At the end of the feedback operation, we conclude the sequence by checking the cavity state. Instead of relying on information provided by K, we perform an independent reconstruction of the average photon-number distribution $p(n)$. The principle of this method, outlined in [20] and investigated in detail in [21], is recalled in the next paragraph.

F. Reconstruction of photon-number distribution

The simplest approach to a measurement of $p(n)$ is to determine, in each realization of the sequence, the actual photon number by a full-fledged QND measurement [16]. This method requires the detection of about 100 atoms, in a time of the order of 25 ms. This relatively long acquisition time is well adapted to the measurement of slowly evolving photon-number distributions, such as that of a coherent state. It is not compatible with states close to a Fock state $|n_t\rangle$, whose $p(n)$ notably evolves over a time of the order of T_c/n_t.

We thus give up determining the photon number in each realization. Instead, we reconstruct by a maximum likelihood (MaxLik) procedure [22] the average photon-number distribution $p_{\rm QND}(n,t=0)$ immediately after the end of the feedback sequence (taken as the time origin in this section). We use information provided by the atoms detected in a 20-sample time window (duration of 1.64 ms after $t=0$) in each of the 4000 realizations of the sequence. The phase of the Ramsey interferometer ϕ_r alternates for successive samples between four values, typically 1.17, 0.36, −0.44, and −1.24 rad. These four phases provide equal sensitivity to eight consecutive photon numbers, e.g., between 0 and 7. We then get a MaxLik estimate of $p_{\rm QND}(n,0)$ [21].

The statistical noise on this estimate is, however, larger than the required precision. Increasing the duration of time window would not help since relaxation comes into play on a longer time scale. We thus instead reconstruct the time evolution of the photon-number distribution $p_{\rm QND}(n,t)$, over a typically 20-ms duration, using a sliding 20-sample time window. The observed noisy evolution is fitted on the predictions of the master equation (2) using the initial $p_{\rm QND}(n)$ values as the only fit parameters and *a priori* knowledge of the independently measured T_c and $n_{\rm th}$, defining the cavity relaxation. We have estimated in [21] the fidelity of this reconstruction method, using extensive numerical simulations. For a state close to $|n_t\rangle$, the statistical uncertainty on $p_{\rm QND}(n_t)$ is about 3%.

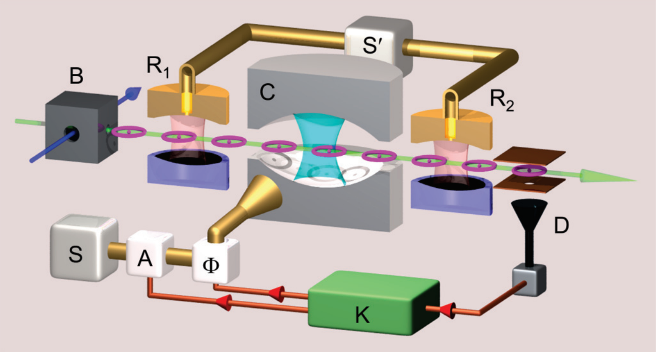

FIG. 3. (Color online) Scheme of the quantum feedback experiment with a classical actuator (coherent microwave injection). K: feedback controller; S: microwave source coupled to C; A and Φ: amplitude and phase controls for microwave injection.

III. FEEDBACK WITH CLASSICAL ACTUATOR

A. Classical source field injection

In the first quantum feedback experiment, proposed in [23], reported in [14], and sketched in Fig. 3, we use as actuator a coherent classical source S. It produces coherent pulses, which are weakly coupled into the cavity mode by diffraction on the mirrors' edges. This injection performs on the cavity state a unitary transformation described by the displacement operator $D(\alpha)=\exp(\alpha a^\dagger - \alpha^* a)$, where α is the *a priori* complex injected amplitude.

In order to speed up the feedback convergence, we prepare, at the beginning of each experimental sequence, the field in a coherent state $\rho_0 = |\alpha_0\rangle\langle\alpha_0|$ of amplitude $\alpha_0=\sqrt{n_t}$. Without loss of generality, we can use this amplitude as the phase reference and hence take it real. This state is produced by S from the vacuum state generated by the absorbing atoms in the first part of the sequence. It has, among all classical states, the largest population in the target state $|n_t\rangle$.

The initial cavity state $|\alpha_0\rangle$ is described by a real density operator, as well as the target Fock state $|n_t\rangle$. The superoperators $\mathbb{T}$ and $\mathbb{M}_\mu^{sn}$ involved in the state estimation have only real elements. We can thus restrict to real values the small amplitudes α injected in each feedback loop by S which acts as actuator. This leads obviously to a considerable simplification of the real-time computations (all matrices are real) and also makes the control of the injection phase technically much simpler.

The real injected amplitude α is controlled by K, based upon its cavity state estimation and upon an optimization made to drive the cavity field as close to the target state as possible.

These procedures are described in more detail in the following paragraphs. The modulus of α is controlled by adjusting the injection duration t_{S} by means of the microwave switch A (a PIN diode). Keeping the output power of S constant, $|\alpha|$ is proportional to t_{S}. In the experiments presented here, $|\alpha| = 0.1$ corresponds to $t_{\mathsf{S}} = 63\ \mu$s. The phase shifter Φ sets the phase of α to zero or π. For a detailed description of this procedure, see Appendix A 3.

The pulse produced by S must be rather intense, even for a small injected amplitude, due to its weak coupling with C. It fills the whole experimental setup, i.e., all the way from B to D, with many microwave photons. We have carefully checked that this rather intense field does not affect the state of all atomic samples flying through the apparatus during injection.

In most feedback loops, the optimal injection has a small amplitude modulus $|\alpha| \ll 1$, as will be shown in Sec. III E1 and in Fig. 9. We therefore decided to limit $|\alpha|$ to $\alpha_{\max} = 0.1$. This enables us to use an approximate form of the displacement operator making the amplitude optimization by K much faster. Furthermore, we do not apply microwave pulses shorter than $0.63\ \mu$s, corresponding to injection amplitudes smaller than $\alpha_{\min} = 0.001$, since their contribution to the field state is much smaller than that of relaxation during the loop duration $T_{\rm a}$. Thus, all applied injections are limited to $|\alpha| \in [\alpha_{\min},\alpha_{\max}]$.

B. Measurement settings

We typically have for the atomic sensors a phase shift per photon $\phi_0 = 0.256\pi$. It makes possible to discriminate all photon numbers from 0 to 7 and is thus quite appropriate for the stabilization of Fock states up to $n_{\rm t} = 4$ reported in this section.

The sensor samples must be as sensitive as possible to a jump out of the target state $|n_{\rm t}\rangle$ into the neighboring Fock states $|n_{\rm t} \pm 1\rangle$. This is achieved by setting the Ramsey interferometer phase to $\phi_{\rm r} = \pi/2 - (n_{\rm t} + 1/2)\phi_0$, leading to equal probabilities for detection of states $|e\rangle$ and $|g\rangle$ in the target state (mid-fringe setting) and to very different detection statistics for states $|n_{\rm t} \pm 1\rangle$. We use this phase setting for stabilizing $|n_{\rm t} = 1\rangle$ and $|n_{\rm t} = 2\rangle$.

For the higher and thus shorter-lived target states $|n_{\rm t} = 3\rangle$ and $|n_{\rm t} = 4\rangle$, this choice is not optimal, as has been observed experimentally. Due to the low thermal photon number ($n_{\rm th} = 0.05$), most quantum jumps from $|n_{\rm t}\rangle$ occur towards $|n_{\rm t} - 1\rangle$. In addition, the coherent displacements applied to correct for a jump widen the initially peaked photon-number distribution. There is thus a finite probability that the correction and the simultaneous QND measurements by the sensors drive the field towards $|n_{\rm t} - 2\rangle$ instead of $|n_{\rm t}\rangle$. Therefore, in order to help K to detect faster these more frequent jumps as well as to correct more efficiently for them, we alternate the Ramsey phase between the two values $\phi_{\rm r,1} = \pi/2 - (n_{\rm t} + 1/2)\phi_0$ and $\phi_{\rm r,2} = \pi/2 - (n_{\rm t} - 1/2)\phi_0$, corresponding to a maximum sensitivity centered at $n_{\rm t}$ and $n_{\rm t} - 1$, respectively. Note that we can not use the phase $\phi_{\rm r,2}$ all the time, as we have seen experimentally and in numerical simulations. In this case, optimized for detecting the population in $|n_{\rm t} - 1\rangle$, the sensors were not able to detect properly the population in the target state $|n_{\rm t}\rangle$, thus reducing the efficiency of the feedback convergence.

C. Quantum state estimation

The state estimation in the loop number k, initiated at the detection of the kth atomic sample in the sequence, takes into account all available information. It includes the measurement results $\{\mu_i'\}$ obtained so far ($1 \leqslant i \leqslant k$) and described by the superoperators $\{\mathbb{M}^{sn}_{\mu_i'}\}$, the action of the next s not yet detected samples flying between C and D, the field decoherence given by the superoperator $\mathbb{T}$ and all applied injections $\{\alpha_i\}$ into C described by the superoperators $\mathbb{D}_{\alpha_i}$:

$$\mathbb{D}_{\alpha_i}\rho = D(\alpha_i)\rho D(-\alpha_i). \tag{19}$$

After detection of the sample k and just before K is ready to apply the feedback injection α_k, the estimated field state reads as

$$\rho_k = \prod_{i=k+1}^{k+s} \left(\mathbb{D}_{\alpha_{i-s}}\mathbb{T}\mathbb{N}\right) \prod_{i=1}^{k} \left(\mathbb{D}_{\alpha_{i-s}}\mathbb{T}\mathbb{M}^{sn}_{\mu_i'}\right) \rho_0. \tag{20}$$

Here, we set $\mathbb{D}_{\alpha_{i-s}}$ to unity for $i \leqslant s$ (no injection is applied before the first sample has been detected) and for $i = k + s$ (after the detection of the last sample k no injection has been performed yet). The right product in (20) includes the detection results of the k already detected samples, and the left product includes the s samples still flying from C to D. Note that here, we implicitly assume that relaxation can be treated independently from displacements and atom-cavity interaction. This is a quite reasonable assumption since the effect of relaxation during the time interval $T_{\rm a}$, represented by the superoperator $\mathbb{T}$, is very small.

In order to make it possible for K to complete the state estimation within a time interval shorter than $T_{\rm a}$, we simplify matrix calculations. First, we truncate the Hilbert space. We limit it to the first Fock states up to $n_{\max} = 7$ photons for the target states $|n_{\rm t} = 1\rangle$ and $|n_{\rm t} = 2\rangle$ and to $n_{\max} = 8$ photons for $|n_{\rm t} = 3\rangle$ and $|n_{\rm t} = 4\rangle$. These values have been experimentally found to be a reasonable compromise between the computation time and the precision of the state estimation.

The next optimization is to compute the superoperator $\mathbb{T}$ using the approximate form given by (3). In addition, the restriction to small (less than 0.1 in modulus) real injection amplitudes allows us to use a second-order approximation in α for the displacement superoperators $\mathbb{D}_\alpha$:

$$\mathbb{D}_\alpha\rho \approx \rho - \alpha[\rho,a^\dagger - a] + \frac{\alpha^2}{2}[[\rho,a^\dagger - a],a^\dagger - a]. \tag{21}$$

We next approximate the left product in (20) by

$$\prod_{i=k+1}^{k+s} \left(\mathbb{D}_{\alpha_{i-s}}\mathbb{T}\mathbb{N}\right) \approx \mathbb{D}_{\beta_k}(\mathbb{T}\mathbb{N})^s \tag{22}$$

with $\beta_k = \sum_{i=k+1-s}^{k-1} \alpha_i$. This approximation holds for small accumulated field displacements $\beta_k \ll 1$ and short delays $sT_{\rm a} \ll T_{\rm c}$. In this way, K precalculates the constant superoperators $\mathbb{M}^{sn}_{\mu'}$, $\mathbb{T}$, and the product $(\mathbb{T}\mathbb{N})^s$ before the feedback operation starts. In each feedback loop, K recursively updates the right product in (20), calculates β_k, and multiplies all resulting operators.

Finally, in order to skip unnecessary operations (e.g., calculation of equal elements or multiplications by zero), we use the intrinsic mathematical properties of the superoperators (symmetries, multidiagonal form, etc.).

D. Controller decision

1. Distance to target

In each loop, the feedback controller K adjusts the value of the control injection α minimizing an appropriate distance between the target and the current state of the system. The distance between any state ρ and a pure quantum reference state ρ_t is often defined as $1 - F_t(\rho)$, where $F_t(\rho) = \mathrm{Tr}\,(\rho\rho_t)$ is the fidelity with respect to the reference state. For $\rho = \rho_t$, the fidelity reaches its maximum value 1, and the distance vanishes. For all states orthogonal to ρ_t, this distance takes its maximum value 1, making it impossible to distinguish between all of them. In other words, this simple distance definition gives no clue on how far from the target the system state is.

We thus provide K with a sensitivity to the photon-number values by defining the distance to the target state $\rho_t = |n_t\rangle\langle n_t|$ as

$$d(\rho_t,\rho) = \mathrm{Tr}\big[\mathfrak{D}_{n_t}\rho\big] \tag{23}$$

with the diagonal distance matrix $\mathfrak{D}_{n_t}$ given by

$$\mathfrak{D}_{n_t} = \sum_{n=0}^{n_{\max}} d_{n_t}(n)\,|n\rangle\,\langle n|\,. \tag{24}$$

Note that this distance reduces to the fidelity-based one $1 - F_t(\rho)$ if $d_{n_t}(n) = 1 - \delta_{n,n_t}$, i.e., if all coefficients are set to 1 except for $d_{n_t}(n_t) = 0$. Figure 4 presents four sets of $d_{n_t}(n)$ coefficients chosen for the stabilization of the four target states $|n_t\rangle$ with n_t ranging from 1 to 4.

At each feedback iteration, after obtaining the updated field state estimate ρ, we search for the displacement amplitude α minimizing $d(\rho_t,\rho_\alpha)$ for the displaced state $\rho_\alpha = \mathbb{D}_\alpha\rho$. The dependence of $d_{n_t}(n)$ is thus chosen to provide a minimum of $d(\rho_t,\rho_\alpha)$ with respect to α in the vicinity of $\alpha = 0$ for $\rho = \rho_t$ and local maxima for all other photon-number states [23]. The exact values of the $d_{n_t}(n)$ coefficients plotted in Fig. 4 are then optimized for each n_t by numerical simulation of the quantum feedback experiment. The optimization criterion is the rate of convergence towards the target state. The principle of these quantum Monte Carlo simulations is outlined in Appendix B.

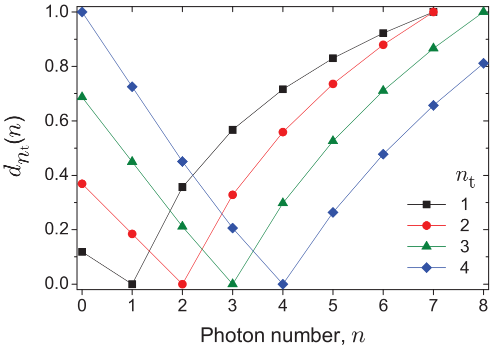

FIG. 4. (Color online) Coefficients $d_{n_t}(n)$ defining the distance $d(\rho_t,\rho)$ to four target Fock states $\rho_t = |n_t\rangle\,\langle n_t|$ with $n_t = 1$ to 4.

2. Determination of the control injection amplitude

Complete numerical minimization of $d(\rho_t,\rho_\alpha)$ with respect to the displacement amplitude α is far too time consuming to be performed by K in the limited duration T_a of a loop. We thus use an analytical approximate formula for the optimal value α_{opt}. Using the second-order approximation of the displacement operators given in (21), we get

$$d(\rho_t,\rho_\alpha) \approx d(\rho_t,\rho) - a_1(\rho)\alpha - a_2(\rho)\frac{\alpha^2}{2} \tag{25}$$

with

$$\begin{aligned} a_1(\rho) &= -\mathrm{Tr}([\mathfrak{D}_{n_t},a^\dagger - a]\rho),\\ a_2(\rho) &= -\mathrm{Tr}([[\mathfrak{D}_{n_t},a^\dagger - a],a^\dagger - a]\rho). \end{aligned} \tag{26}$$

The optimal amplitude α_{opt} must minimize the second-order polynomial function in (25) over the interval $[-\alpha_{\max},\alpha_{\max}]$. If $a_2(\rho) < 0$, $d(\rho_t,\rho_\alpha)$ is convex and reaches its minimum for $\alpha_{\mathrm{opt}} = -a_1(\rho)/a_2(\rho)$. If this value falls outside the allowed interval, or if $a_2(\rho) \geqslant 0$ meaning that the concave $d(\rho_t,\rho_\alpha)$ function has no local minimum, we set α_{opt} to the interval margin $\pm\alpha_{\max}$ corresponding to the smallest distance, i.e., $\alpha_{\mathrm{opt}} = \mathrm{sgn}[a_1(\rho)]\alpha_{\max}$. Moreover, if $|\alpha_{\mathrm{opt}}| < \alpha_{\min}$, K sets $\alpha_{\mathrm{opt}} = 0$ (see Sec. III A).

The total duration of the calculations performed by K for a single loop never exceeds 70 μs. We thus programmed K to switch the required correction phase by the phase shifter Φ always at 70 μs after the loop start. At the same moment K also opens the switch A which is then closed after the injection duration corresponding to the chosen amplitude modulus $|\alpha_{\mathrm{opt}}|$. This duration being limited to $\alpha_{\max} = 63$ μs, the microwave pulses of neighboring feedback loops never overlap.

Aside from numerical simulations, which have been extensively used to test and optimize the feedback algorithm, the convergence of the closed-loop system in the presence of the experimental imperfections has also been confirmed theoretically by considering $d(\rho_t,\rho)$ as a control Lyapunov function [24] and ensuring global asymptotic convergence towards the target state ρ_t in the absence of decoherence [25].

E. Experimental results

1. Examples of individual trajectories

Figure 5 presents two individual feedback sequences corresponding to $n_t = 1$ and 4. The panels, from top to bottom, present the atomic detection results (the bars indicate the number of detected atoms in g and e in each loop), the distance d to the target ρ_t, the injection amplitude α chosen by K and plotted in a pseudologarithmic scale with an excluded interval $]-0.001,0.001[$, and the estimated photon-number distribution $p(n)$ in color (grayscale). The evolution of the mean photon number $\overline{n}$ is shown as a black line in the $p(n)$ panel. Figure 6 shows four density matrices estimated by K at times $t = 0$, 15.6, 48.4, and 51.5 ms during the feedback sequence presented in Fig. 5 for $n_t = 4$ (right panel).

Starting from the coherent field with amplitude $\alpha_0 = \sqrt{n_t}$, the field state converges rapidly to the target, with a $p(n_t)$ value close to one and hence $\overline{n} \approx n_t$. The actuator then idles since this is the best strategy to keep the prepared state. From time to

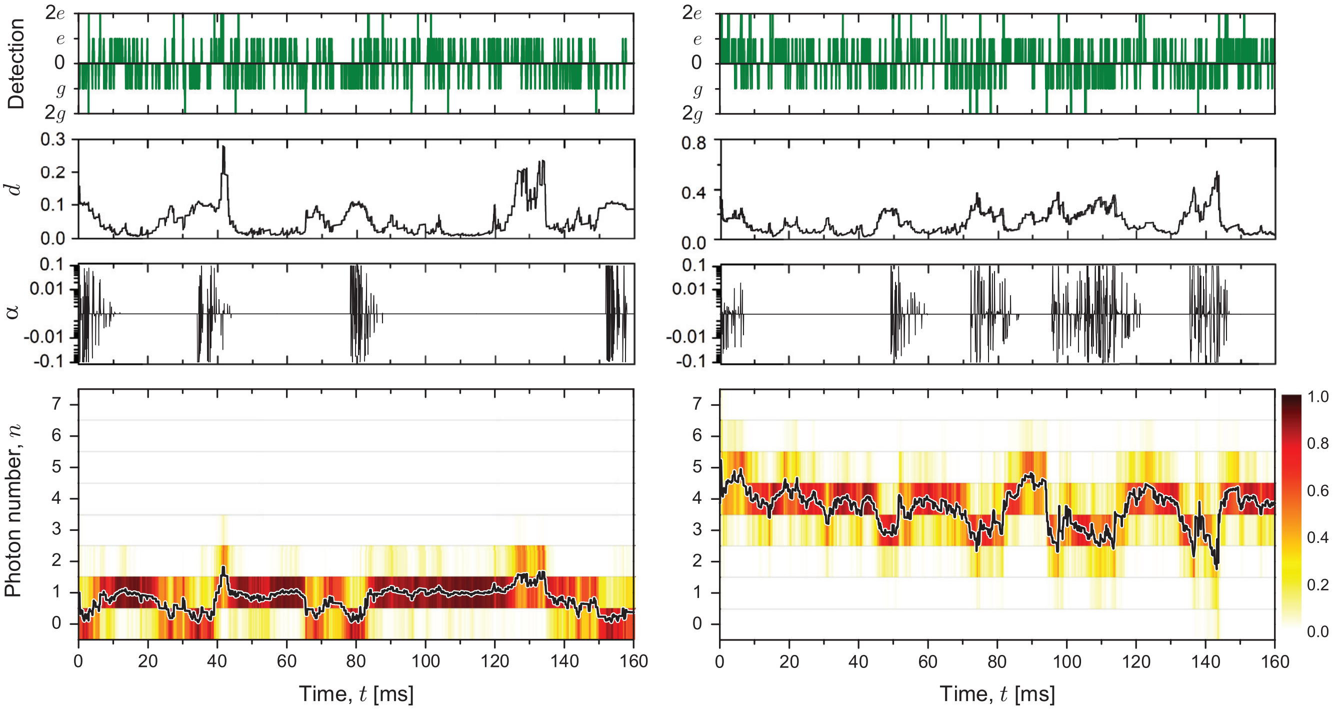

FIG. 5. (Color online) Single sequences of the feedback experiment with $n_t = 1$ (left panel) and $n_t = 4$ (right panel). The frames present as a function of time t the detected sensor states (upwards bars for e, downwards bars for g), the distance d to n_t, the feedback injection amplitude α chosen by K (in pseudologarithmic scale), and the photon-number distribution $p(n)$ inferred by K [color (grayscale)] together with its mean value $\overline{n}$ (solid black line).

time, K detects a quantum jump. This is for instance the case at 23 ms (photon loss) and 125 ms (thermal excitation creation) for $n_t = 1$ in Fig. 5. The average photon number progressively changes as information is gathered from the sensor atoms, and the distance d accordingly increases. The controller thus reactivates the actuator and S injects correcting microwave fields to restore $|n_t\rangle$.

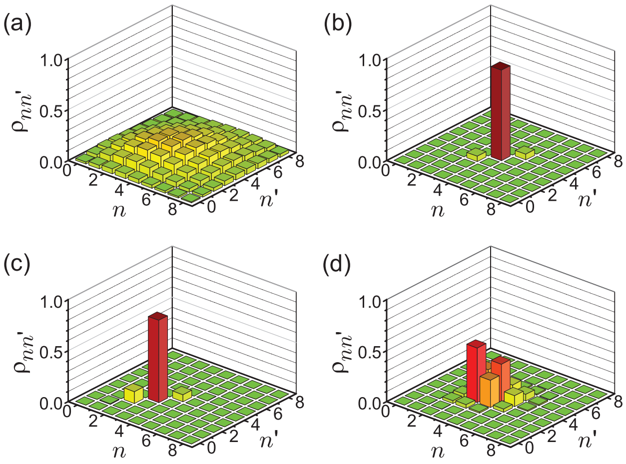

FIG. 6. (Color online) Absolute values of the cavity field density matrix elements estimated by the controller during the realization of the feedback experiment with $n_t = 4$ presented in Fig. 5 (right panel). (a) Initial coherent state ($t = 0$ ms) with the average photon number n_t. (b)–(d) Estimated state at 15.6 ms (high population in $|n_t\rangle$ after initial feedback convergence), at 48.4 ms (after a sudden quantum jump to $|n_t - 1\rangle$), and at 51.5 ms (during the correction phase), respectively.

We clearly observe that the correction of a single quantum jump implies very many actions of the actuator source S. Acting alone, S would produce a coherent displacement with a well-defined phase. In contrast, we need compensate a single photon loss or creation, implying no phase information at all. The feedback strategy, spontaneously implemented by K, consists in performing many injections with exponentially decaying amplitudes of two opposite phases, as conspicuous in Fig. 5. The interplay between these injections and the state reductions performed by the sensor atoms results in an effective phaseless injection or subtraction of a single photon.

The corrections are more frequent when the target photon number increases since its lifetime decreases, making quantum jumps more frequent. For $n_t = 4$, as clearly seen in Fig. 5, the actuator is active up to 50% of the time. This indicates why higher n_t values can not be stabilized with this coherent feedback scheme.

2. *Average evolution of* $p(n)$

Figure 7 shows the time evolution of the average probabilities $\overline{p}(n_t,t)$, $\overline{p}(n < n_t,t)$, and $\overline{p}(n > n_t,t)$ to have n_t, less than n_t, and more than n_t photons in the field, respectively, for each target state $n_t = 1$ to 4. The averages are performed over 4000 sequences. After a few tens of milliseconds, these probabilities saturate to their steady-state values set by the competition between the quantum jumps out of the target state and the state recovery induced by the feedback mechanism.

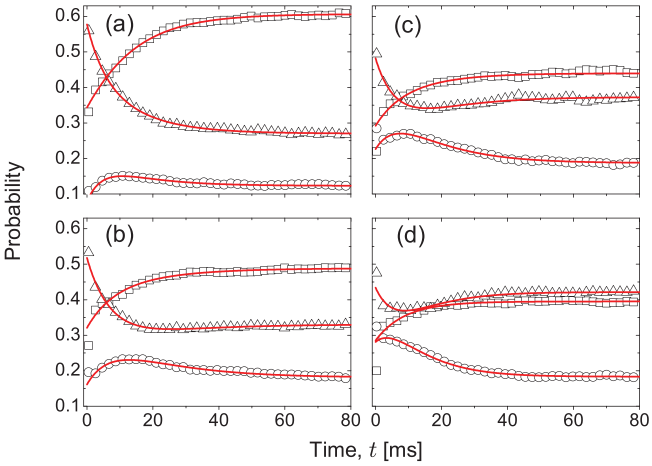

FIG. 7. (Color online) Establishment of the steady-state regime. The probabilities $\overline{p}(n_t,t)$ (squares), $\overline{p}(n < n_t,t)$ (triangles), and $\overline{p}(n > n_t,t)$ (circles) are averaged over 4000 trajectories for each n_t value. Panels (a) to (d) correspond to $n_t = 1$ to 4, respectively. Solid lines are a fit with the sum of two exponential functions.

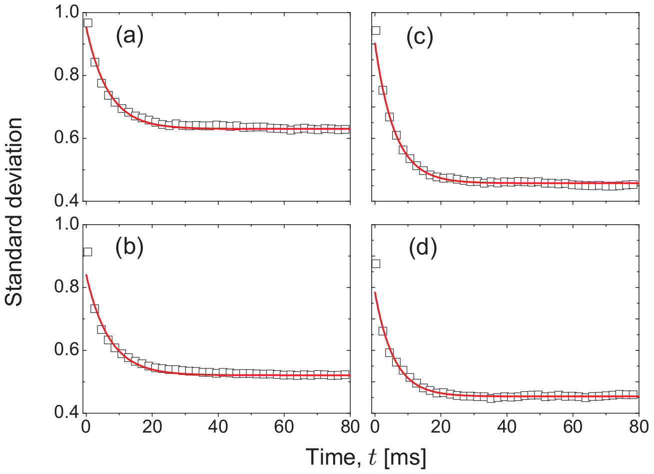

FIG. 8. (Color online) Time evolution of the normalized standard deviation $\overline{\sigma}(t)$ averaged over 4000 trajectories for each n_t value. Panels (a) to (d) correspond to $n_t = 1$ to 4, respectively. Solid lines are fits to an exponential decay.

For each target state, the probabilities fit well with the sum of two exponential functions with time constants t_1 and t_2. They are given in Table II for all n_t values. We identify the reciprocal of the first time constant t_1^{-1}, with the rate of information acquisition by the sensor atoms. Acting alone, this information gathering process would project the cavity field onto a randomly selected Fock state in a time of the order of t_1 [16]. The second time constant corresponds to the time required to inject or suppress individual photons in the cavity. It is quite long and $t_2 > t_1$ since, as mentioned above, the injection of a single photon requires very many actions of S.

The evolution of the average standard deviation $\overline{\sigma}(t)$ of the photon-number distributions $p(n,t)$ performed on the same 4000 trajectories for each n_t value is shown in Fig. 8. The monotonic reduction of $\overline{\sigma}(t)$ fits well with an exponential decay with a single time constant t_σ given in Table II. The photon-number variance reduction is mostly linked to the rate of information provided by the sensor atoms and fairly insensitive to the actuator's injections, which do not broaden $p(n)$ on the average. Hence, we get a single time constant t_σ with $t_\sigma \approx t_1$.

3. Controller actions

Figure 9 presents an analysis of the feedback injections chosen by K during all sequences with $|n_t = 4\rangle$. Figure 9(a) shows the histogram of all nonzero values of the injection amplitude α in a pseudologarithmic scale, obtained from 4000 feedback sequences. About 50% of these amplitudes are inside the interval $[-0.01,0.01]$ and only 25% have the maximum allowed modulus $\alpha_{\max} = 0.1$. Our choice for $\alpha_{\max}$ is thus justified *a posteriori*. Since all injection amplitudes from the interval $]-\alpha_{\min},\alpha_{\min}[$ are arbitrarily set to zero, we have excluded it from the plot.

TABLE II. Characteristic times, in milliseconds, of the establishment of the steady-state regime.

n_t	1	2	3	4
t_1	4.9 ± 0.1	7.4 ± 0.1	6.7 ± 0.2	6.8 ± 0.3
t_2	13.7 ± 0.1	18.8 ± 0.2	14.2 ± 0.3	9.9 ± 0.3
t_σ	6.39 ± 0.04	7.00 ± 0.05	6.02 ± 0.02	5.78 ± 0.04

Figure 9(b) presents the average correction amplitude $\overline{|\alpha|}$ as a function of the estimated probability $p(n_t)$. As intuitively expected, the higher $p(n_t)$, the smaller $\overline{|\alpha|}$. For very small

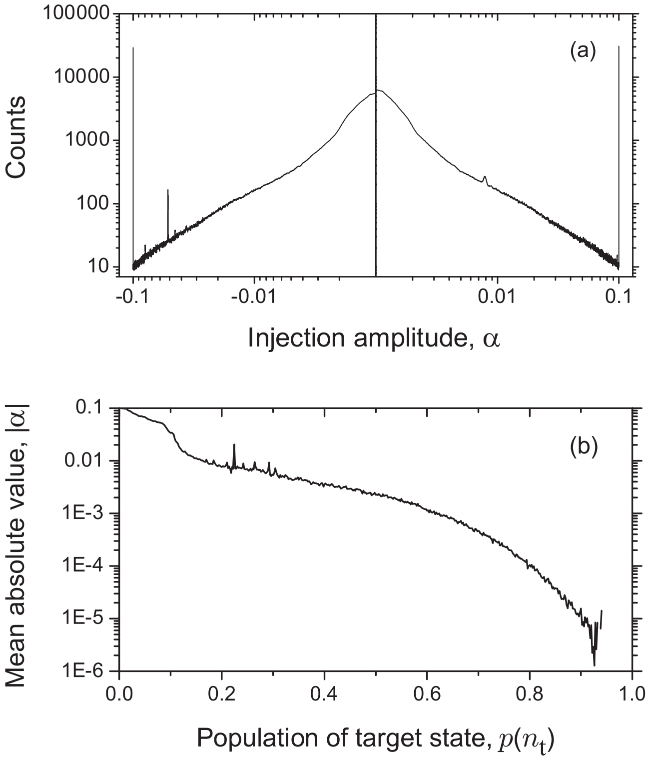

FIG. 9. Injection amplitudes chosen during feedback operation with $|n_t = 4\rangle$. (a) Histogram of nonzero values of α. (b) Absolute value of α averaged over 4000 trajectories of 164 ms duration as a function of the current probability of n_t.

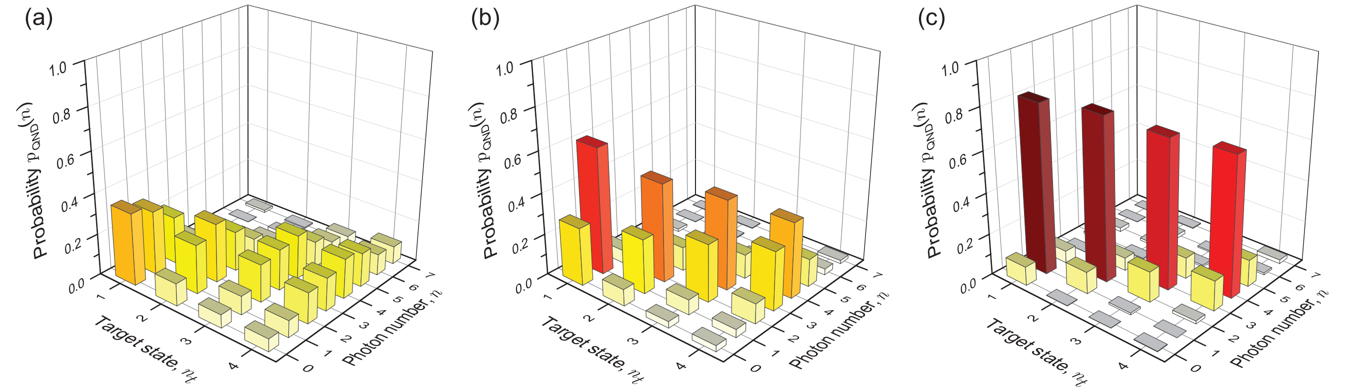

FIG. 10. (Color online) Photon-number distribution $p_{\mathrm{QND}}(n)$, measured by an independent QND process, for the target photon numbers n_t from 1 to 4 prepared by means of the coherent actuator feedback. (a) Reference initial coherent field with n_t photons on the average. (b) Field reconstructed in the steady-state mode after interrupting the feedback loop at 164 ms. (c) Converged field when K estimates that $p(n_t) > 0.8$.

values of $p(n_t)$, the cavity is far from the target state and almost all injections have the largest allowed modulus 0.1.

The conspicuous peak at $\alpha = -0.05$ in Fig. 9(a) results from our initial state choice, a coherent state with an amplitude $\alpha_0 = 2$ (4 photons on the average). It corresponds to a maximum value for $p(n_t)$. However, it does not correspond to a minimum of the distance defined in Fig. 4. In fact, this distance of a coherent state to the target is minimal for an amplitude $\alpha_d = \sqrt{3.8}$. Thus, K, aware of the initial state, starts by correcting in the first loop this mismatch by injecting an amplitude $\alpha_{\mathrm{opt}} = \alpha_d - \alpha_0 = -0.05$. At this initial time, $p(n_t) = 0.22$, explaining the small peak at this value in Fig. 9(b).

4. Photon-number distribution of prepared states

As discussed in Sec. II F, we assess the feedback performance in the steady-state and convergence modes by reconstructing the photon-number distributions $p_{\mathrm{QND}}(n)$ at the end of the feedback procedure. Figure 10 shows three measured distributions: (a) that of the initial coherent field; (b) the steady-state distribution after interrupting the feedback operation after 164 ms; (c) the distribution after feedback convergence [$p(n_t) \geqslant 0.8$].

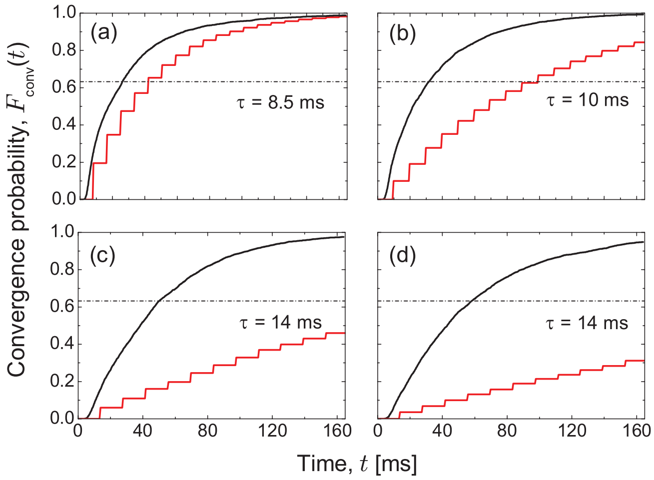

FIG. 11. (Color online) Probability $F_{\mathrm{conv}}(n_t,t)$ for $p(n_t)$ to reach a threshold level of 0.8 (smooth line). Panels (a) to (d) correspond to n_t from 1 to 4. Each curve is determined from 4000 trajectories. The horizontal lines depict the 0.63 level defining the convergence time. The staircase line presents a passive trial-and-error QND method for Fock state preparation.

The feedback conspicuously narrows the photon-number distribution and considerably increases the target state population. In the steady state, for all n_t values, $p_{\mathrm{QND}}(n_t)$ is about twice as high as the initial value in the coherent state. Of course, the higher the photon number, the higher the probability for halting the feedback during a quantum jump recovery. This explains the lower performance observed for high-lying states.

In the convergence mode, the target state population is obviously much higher since we never halt feedback during a quantum jump recovery in principle. The final $p_{\mathrm{QND}}(n_t)$ is very close to the threshold value for low n_t. It departs from it for the higher n_t due to the finite time required by K to detect a quantum jump.

5. Convergence time

We deduce from the analysis of all 4000 feedback sequences in the convergence mode the probability $F_{\mathrm{conv}}(n_t,t)$ for $p(n_t)$ to reach the threshold 0.8 at time t. Figure 11 shows the corresponding results for the four target states. We define the convergence time for each n_t value as the time for which $1 - e^{-1} = 63\%$ of the sequences converge. The convergence times correspond to the intersection of the $F_{\mathrm{conv}}(n_t,t)$ curves with the horizontal lines in Fig. 11. They are given in Table III.

It is instructive to compare our active feedback scheme with a simpler, passive method providing us with a Fock state $|n_t\rangle$ on demand. It is based on a "trial-and-error" approach. We prepare a coherent state with an amplitude $\alpha_0 = \sqrt{n_t}$.

TABLE III. Convergence time, in milliseconds, of two protocols preparing photon-number states $|n_t\rangle$ on demand.

n_t	1	2	3	4
Coherent injection feedback	26	31	49	58
Trial-and-error projection	42	89	251	418

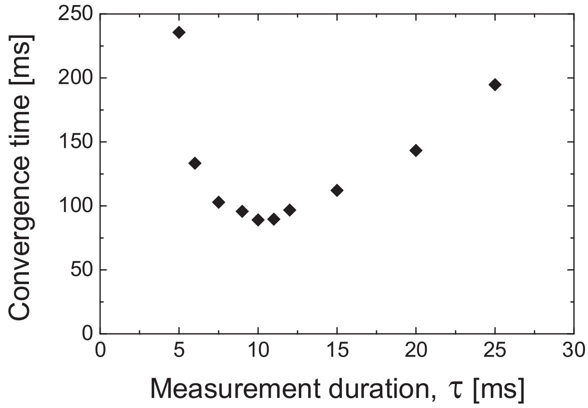

FIG. 12. Optimization of the QND measurement duration of the trial-and-error Fock state preparation for $n_t = 2$.

We then send dispersive sensors for a total time τ. Their settings (Ramsey phase and dephasing per photon) are the same as for the feedback sensors, i.e., to optimally distinguish the n_t-photon state from the others (see Sec. III B). If we get from this measurement $p(n_t) \geqslant 0.8$, we have succeeded. If it is not the case, we erase the cavity field and restart the whole preparation-measurement sequence. We adjust the measurement time τ by minimizing the overall convergence time (see Fig. 12 for $n_t = 2$). If τ is chosen to be too short, the sensors do not bring enough information to pick up a definite photon number. If τ is very long, the overall convergence time, which is basically the product of the average number of trials [at least of the order of $1/p(n_t)$ in the initial coherent state] by their duration τ, is also very long.

The optimized values of τ for the four n_t values and the corresponding convergence probabilities are also shown in Fig. 11. The convergence times of both the feedback and trial-and-error state preparations are summarized in Table III. Note that we do not include into τ the time needed to restart a new sequence, thus overestimating the efficiency of the passive method. Being about 1.6 times faster for $n_t = 1$, the feedback method becomes more and more efficient with respect to the passive one for higher n_t.

This clearly demonstrates the interest of an active method even for the simple task of state preparation. Of course, the passive method is totally unable to preserve the prepared Fock state by compensating for the quantum jumps.

IV. FEEDBACK WITH QUANTUM ACTUATORS

A. Resonant atoms in a feedback loop

We now use resonant atoms as the feedback actuators for the correction of quantum jumps. The scheme of this experiment is presented in Fig. 13(a). Its general organization is similar to that of the coherent feedback experiment. Here, however, Rydberg atoms are used both as sensors extracting QND information out of the field and as actuators correcting the field quantum jumps. The actuator atoms can either emit a single photon into the mode or absorb one, according to their initial state ($|e\rangle$ or $|g\rangle$). This scheme allows us to perform fast correction of quantum jumps and to stabilize high-lying Fock states, up to $n_t = 7$.

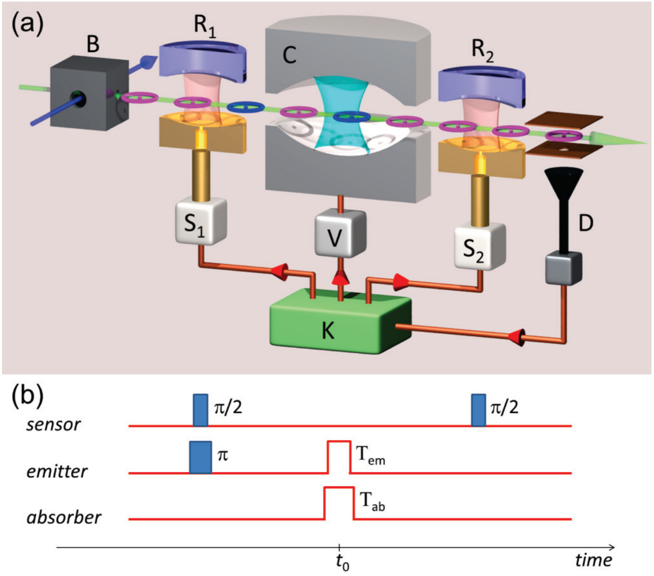

FIG. 13. (Color online) Scheme of the quantum feedback experiment with emitting and absorbing resonant atoms used as quantum actuators. (a) Experimental setup. The controller K sets the durations of the microwave pulses in R_1 and R_2 and the potential V applied to one of the mirrors of C. Light (magenta) and dark (blue) toroids represent sensor (dispersive) and actuator (resonant) samples. Their positions with respect to the Ramsey zones, cavity, and detectors are to scale. They correspond to the end of the kth feedback loop after the detection of atom k. (b) Schematic control sequence for the realization of the three atomic sample types for an atom crossing the cavity center at time t_0. The rectangles represent the Ramsey pulses. The solid line represents the time dependence of the potential V, which is switched between two values V_{dis} (lower) and V_{res} (upper), corresponding to dispersive and resonant atom-field interaction, respectively.

1. Three atomic sample types

An atomic sample can be either set as a sensor (sn), an emitter (em), or an absorber (ab), corresponding respectively to three atomic states at the entrance of C: $(|g\rangle + |e\rangle)/\sqrt{2}$, $|e\rangle$, and $|g\rangle$. Since all atoms exit the circular state excitation zone B in $|g\rangle$, the preparations of a sensor, an emitter, or an absorber require a $\pi/2$ pulse, a π pulse, or no pulse at all in R_1, respectively, as schematically shown in Fig. 13(b).

Sensors interact dispersively with C before undergoing a second $\pi/2$ Ramsey pulse in R_2. Actuators are set at resonance with C and do not experience a pulse in R_2. The atomic frequency in C, and thus the atom-cavity detuning δ, are controlled by the Stark effect produced by the potential V applied to one of the mirrors (the other is connected to ground). The dispersive ($\delta/2\pi = 245$ kHz) and resonant ($\delta = 0$) conditions correspond to $V = V_{\text{dis}} = -0.62$ V and $V = V_{\text{res}} = -2.5$ V, respectively. The default potential value is V_{dis}. For actuator samples, we thus switch V to V_{res} for the appropriate time interval $T_{\text{res}} = T_{\text{em}}$ or T_{ab}, depending on the actuator type [see Fig. 13(b)]. The application of this potential pulse is synchronized with the atomic position in C. It is centered around the time when the sample crosses the cavity axis.

During the time interval T_{res}, the sample moves across the Gaussian transverse profile of the cavity mode. We take this motion into account by defining the effective atom-cavity interaction time t_{eff}:

$$t_{\text{eff}} = \int_{-\frac{T_{\text{res}}}{2}}^{\frac{T_{\text{res}}}{2}} e^{-(vt/w_0)^2}\, dt. \tag{27}$$

From now on, we always refer to this effective time when discussing resonant interaction.

In principle, the quantum jump compensation could be achieved with a single actuator. On the contrary, each sensor only provides partial information on the photon-number distribution. Many tens of sensors are required to extract a photon number from the binary information provided by atomic detections [16]. We can thus anticipate that an efficient feedback requires many more sensor samples than actuators. We thus alternate, in the feedback sequence, a series of N_{sn} sensor and N_{ct} control samples, with $N_{sn} > N_{ct}$. The typical values are $N_{sn} = 12$ and $N_{ct} = 4$. They have been first found by numerical simulation of the feedback performance (see Sec. IV E3) and then optimized experimentally.

The samples in the sensor group are always used as sensors. The samples in the control group are controlled by K. Based on its state estimation, it can decide to use them as emitters or absorbers. It can also decide, if the state is close to the target, to use them as sensors.

2. *Feedback loop*

The initial field state in this experiment is the vacuum $\rho_0 = |0\rangle\langle 0|$, produced by the field-absorbing atoms at the beginning of each sequence. After each sample detection, K estimates the field's quantum state taking into account the type of the last detected sample. No information is wasted and the final state of emitter and absorber samples is also used in this estimation, as well as all available information on experimental imperfections for dispersive and resonant interactions. Then, K decides which action for the control samples at hand leads to the largest reduction of a proper distance between the estimated and target states.

At the end of the state estimation based on the kth sample detection, there are three samples upon which K decides, provided of course they are of the control type (sensor samples are not under control of K). The sample $k + 8$ is at this time located immediately before R_1. It can still be programmed to be either an emitter, an actuator, or a sensor by choosing its initial state. The samples $k + 7$ and $k + 6$ are flying from R_1 to C. Their states have already been decided upon and can not be modified. However, K can still decide whether it applies the Stark pulse in C or not. It can thus decide to use these samples as actuators, as initially planned, or to merely discard them if new information makes this option optimal. For these discarded (ds) samples, the potential V of the cavity mirror is kept at the value V_{dis} for a dispersive atom-cavity interaction. Within an irrelevant global phase, this interaction does not modify the photon-number distribution and extracts no information. No pulse is applied in R_2 and the result of the final detection in D is merely discarded.

B. Resonant interaction

1. *Rabi oscillations*

The resonant interaction of an atom with the cavity field results in a coherent energy exchange, the quantum Rabi oscillation, well described by the Jaynes-Cummings model [4]. Starting from a joint atom-cavity state $|e,n\rangle$ or $|g,n+1\rangle$, the system evolves, after the effective interaction time t, into $|\Psi^{em}(t)\rangle$ or $|\Psi^{ab}(t)\rangle$ given, respectively, by

$$\begin{aligned} |\Psi^{em}(n,t)\rangle &= \cos\frac{\Omega_n t}{2}|e,n\rangle + \sin\frac{\Omega_n t}{2}|g,n+1\rangle, \\ |\Psi^{ab}(n,t)\rangle &= -\sin\frac{\Omega_n t}{2}|e,n\rangle + \cos\frac{\Omega_n t}{2}|g,n+1\rangle. \end{aligned} \tag{28}$$

Energy exchange between the atom and the field occurs at the frequency

$$\Omega_n = \Omega_0\sqrt{n+1}, \tag{29}$$

where Ω_0 is the vacuum Rabi frequency. From (28) we see that the probability to detect an atom in state $|g\rangle$ oscillates in time as

$$\begin{aligned} \pi_g^{em}(n,t) &= \tfrac{1}{2} - \tfrac{1}{2}\cos(\Omega_n t), \\ \pi_g^{ab}(n,t) &= \tfrac{1}{2} + \tfrac{1}{2}\cos(\Omega_n t). \end{aligned} \tag{30}$$

2. *Experimental imperfections*

Figure 14 shows experimental vacuum Rabi oscillations. To avoid contributions from two-atom events, we have lowered the average atom number per sample and have selected only the sequences in which exactly one atom is detected. We plot the probability $\pi_g(t)$ to detect an atom in state $|g\rangle$ versus the effective interaction time t. In Fig. 14(a), the initial atomic state is $|e\rangle$ and the cavity is initially in its vacuum state. In Fig. 14(b), the initial atomic state is $|g\rangle$ and the cavity contains one photon. This initial one-photon Fock state is prepared by the QND photon-number projection of a small coherent field followed by a post-selection of the experimental runs in which the measured final probability $p(1)$ of having 1 photon is larger than 90% [20]. In this way, we obtain $p(1) = 93.4\%$, close to an ideal Fock state $|n = 1\rangle$.

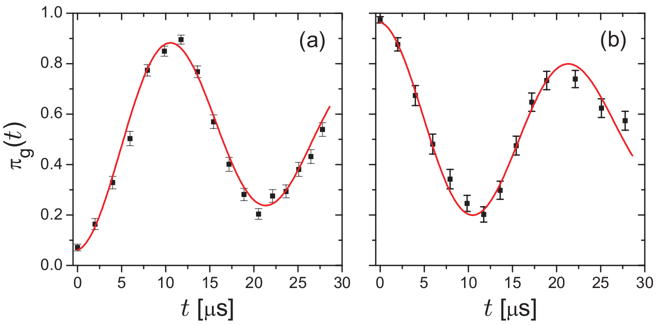

FIG. 14. (Color online) Experimental vacuum Rabi oscillations. The probability π_g to detect a resonant atom in state g is measured as a function of the effective interaction time t. Initially, the atom-cavity system is prepared in a joint state $|e,0\rangle$ (a) or $|g,1\rangle$ (b). The dots are experimental, with statistical error bars. Solid lines are phenomenological fits to exponentially damped oscillating functions.

The experimental Rabi oscillations are damped and have a reduced contrast as compared to the ideal oscillations in (30). The solid lines in Fig. 14 are fits to phenomenological functions including a damping term, given by

$$\begin{aligned} \pi_g^{|e,0\rangle}(t) &= \pi_0 - \frac{c}{2}\, e^{-t/\tau_0} \cos(\Omega_0 t), \\ \pi_g^{|g,1\rangle}(t) &= \pi_0 + \frac{c}{2}\, e^{-t/\tau_0} \cos(\Omega_0 t). \end{aligned} \tag{31}$$

The shared fit parameters are the Rabi frequency $\Omega_0/2\pi = (46.0 \pm 0.3)$ kHz, the damping rate $1/\tau_0 = (0.022 \pm 0.006)\ \mu\mathrm{s}^{-1}$, the offset $\pi_0 = 0.51 \pm 0.01$ and the contrast $c = 0.90 \pm 0.02$. Good agreement between the recorded oscillations and the fit justifies our choice of an exponential damping.

The points at $t = 0$ in Fig. 14 correspond to a direct atomic state detection with no atom-cavity interaction. In principle, the corresponding probabilities should be zero and one in Figs. 14(a) and 14(b), respectively. The observed deviations from these values, and hence the contrast c and offset π_0 of the fit functions, can be attributed to pure detection errors $\tilde{\eta}_e$ and $\tilde{\eta}_g$ mixing the detected states. We can express the contrast and the offset in terms of these errors [see Eq. (16)]:

$$c = 1 - \tilde{\eta}_e - \tilde{\eta}_g, \quad \pi_0 = (1 + \tilde{\eta}_e - \tilde{\eta}_g)/2, \tag{32}$$

resulting in $\tilde{\eta}_g = 0.03 \pm 0.01$ and $\tilde{\eta}_e = 0.07 \pm 0.01$. Note that $\tilde{\eta}_e$ and $\tilde{\eta}_g$ are the real detection errors and not the effective mixing η_e and η_g of the atomic states describing the Ramsey interferometer imperfections, which we introduced in Sec. II C1.

In order to characterize fully the resonant interaction for all relevant photon-number states, we have measured a series of Rabi oscillations starting from joint atom-field states $|e,n\rangle$ $(0 \leqslant n \leqslant 6)$ and $|g,n\rangle$ $(1 \leqslant n \leqslant 6)$. The resulting signals are plotted in Fig. 15 for an initial atomic state $|g\rangle$ (the data corresponding to $|e\rangle$ are not shown for the sake of clarity, but they have also been recorded and analyzed).

The photon-number states $|n\rangle$ are again obtained by a QND photon-number measurement procedure performed on an initial coherent state and by selecting the realizations in which the final probability of having n photons is larger than a threshold f_n. The chosen values of f_n and the resulting photon-number distribution for n from 0 to 6 are given in Table IV. These distributions are mainly a mixture of the required Fock state with its two neighbors and will be taken into account in the following analysis.

TABLE IV. Measured photon-number distribution $p(n)$ of the photon-number states prepared by QND photon counting with the threshold f_n.

n	f_n	$p(n-1)$	$p(n)$	$p(n+1)$
0	0.90		0.97	0.03
1	0.90	0.05	0.93	0.02
2	0.85	0.07	0.89	0.04
3	0.80	0.10	0.85	0.05
4	0.75	0.13	0.80	0.07
5	0.70	0.16	0.76	0.08
6	0.60	0.21	0.68	0.11

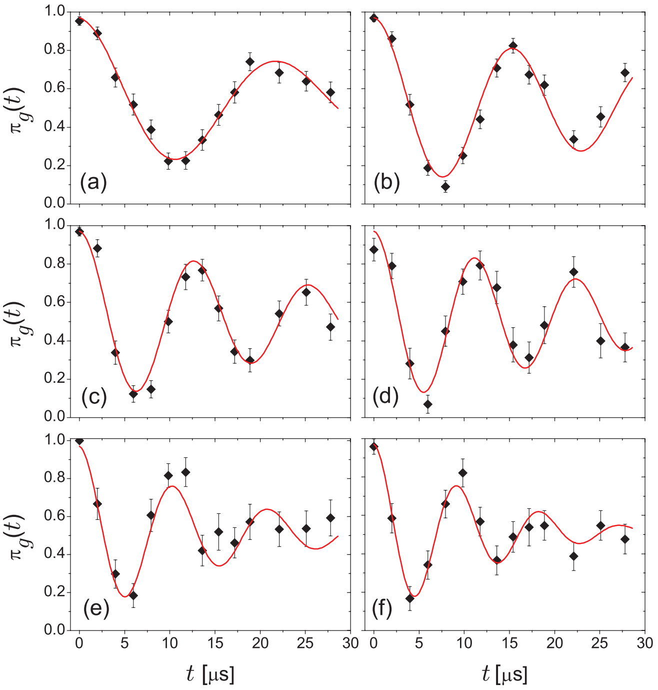

FIG. 15. (Color online) Rabi oscillations measured in Fock states from $n = 1$ (a) to 6 (f). The initial atomic state is $|g\rangle$ (the data for the initial level $|e\rangle$ are not presented in this figure). The points are experimental with statistical error bars. Solid lines are fits to phenomenological damped oscillating functions taking into account the impurity of the prepared Fock states.

We fit the data in Fig. 15 with a sum, over the photon number, of phenomenologically damped Rabi oscillations, weighted by the photon-number probability distributions given in Table IV. These functions, for the Fock state $|n\rangle$ and the initial levels $|e\rangle$ and $|g\rangle$, are given by

$$\begin{aligned} \pi_g^{|e,n\rangle}(t) &= \pi_0 - \frac{c}{2}\, e^{-t/\tau_n} \cos(\Omega_n t), \\ \pi_g^{|g,n\rangle}(t) &= \pi_0 + \frac{c}{2}\, e^{-t/\tau_{n-1}} \cos(\Omega_{n-1} t). \end{aligned} \tag{33}$$

The shared contrast c and offset π_0 are determined by the fits of Fig. 14. The only fit parameters are thus the n-photon Rabi frequencies Ω_n and the damping rates τ_n^{-1}.

The fitted values of these parameters are shown in Fig. 16 as functions of $\sqrt{n+1}$. Squares and rectangles are deduced, respectively, from oscillations starting from $|e,n\rangle$ and $|g,n+1\rangle$.

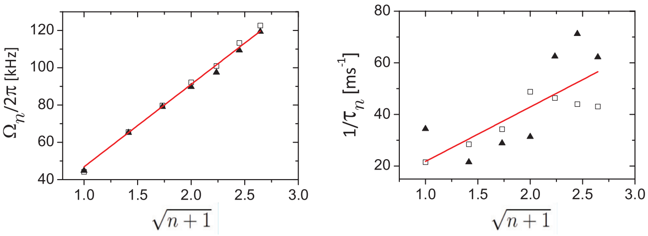

FIG. 16. (Color online) Frequency and damping rate of the fits to the experimental Rabi oscillations. The initial atom-cavity state is either $|g,n+1\rangle$ (triangles) or $|e,n\rangle$ (squares). Straight lines are linear fits.

We observe that Ω_n is, as expected from (29), proportional to $\sqrt{n+1}$. We deduce from these data $\Omega_0/2\pi = 46.0 \pm 0.5$ kHz, in good agreement with the value extracted above from the vacuum oscillations.

More surprisingly, the damping rates τ_n^{-1} are also, within a large experimental dispersion, proportional to $\sqrt{n+1}$:

$$\tau_n^{-1} \approx \tau_0^{-1}\sqrt{n+1}. \tag{34}$$

The τ_0^{-1} value extracted from the linear fit in Fig. 16, $1/\tau_0 = 0.020 \pm 0.009\ \mu\text{s}^{-1}$, coincides with the damping rate of the vacuum oscillations obtained above.

This result suggests that a dominant source of Rabi oscillations damping might be the dispersion of the vacuum Rabi frequencies experienced by atoms crossing C along different paths within the 1-mm diameter of the atomic beam, which is not much smaller than the standing-wave pattern extension along the cavity axis. A simple model of this dispersion effectively leads to a damping rate proportional to the average Rabi oscillation frequency.

The Rabi oscillations are quite sensitive to the experimental alignment, e.g., to the position of the atomic beam with respect to the cavity mode. They are thus regularly recalibrated. The results of Fig. 16 allow us to simplify this calibration by recording only vacuum oscillations $\pi_g^{|e,0\rangle}(t)$ [Fig. 14(a)] and then deducing all Rabi oscillations from this single fit.

3. *Field transformation*

In this feedback scheme, all state transformations, from the field relaxation to the interaction with sensors and actuator atomic samples, do not couple the diagonal elements of the field's density operator ρ (the photon-number probability distribution $p(n) = \rho_{nn}$) to its nondiagonal terms. In other words, all operations performed on the field are phase independent. The initial state being the vacuum, with no phase information, the nondiagonal elements of ρ remain zero during the whole feedback sequence. Therefore, we can greatly simplify the state estimation and controller decision making by only keeping track of $p(n)$. We nevertheless still use, in the following discussion, the density matrix formalism for the sake of an easy comparison of the two feedback methods. We must keep in mind that all density operators are, from now on, diagonal in the Fock state basis.

Let us note R_μ^ν the Kraus operator describing the field projection occurring when an emitter ($\nu = em$) or absorber ($\nu = ab$) atom has been ideally detected in state μ after an ideal resonant interaction with C. Using (28), we obtain the four Kraus operators

$$\begin{aligned}
R_e^{em} &= \sum_n \cos\frac{\Omega_n t}{2}\,|n\rangle\,\langle n|\,,\\
R_g^{em} &= \sum_n \sin\frac{\Omega_n t}{2}\,|n+1\rangle\,\langle n|\,,\\
R_e^{ab} &= \sum_n \sin\frac{\Omega_n t}{2}\,|n\rangle\,\langle n+1|\,,\\
R_g^{ab} &= \sum_n \cos\frac{\Omega_n t}{2}\,|n+1\rangle\,\langle n+1| + |0\rangle\,\langle 0|\,.
\end{aligned} \tag{35}$$

The corresponding state transformation reads as

$$\mathbb{M}_\mu^\nu \rho \equiv \frac{R_\mu^\nu \rho R_\mu^{\nu\dagger}}{\text{Tr}\left(R_\mu^\nu \rho R_\mu^{\nu\dagger}\right)}. \tag{36}$$

In order to take into account the spurious experimental Rabi oscillation damping, we replace the ideal state transformations $R_\mu^\nu \rho R_\mu^{\nu\dagger}$ by the action of the superoperators $\mathbb{R}_\mu^\nu$ given by

$$\begin{aligned}
\left[\mathbb{R}_e^{em}\rho\right]_{nn} &= \tfrac{1}{2}[1 + e^{-t/\tau_n}\cos(\Omega_n t)]\rho_{nn},\\
\left[\mathbb{R}_g^{em}\rho\right]_{nn} &= \tfrac{1}{2}[1 - e^{-t/\tau_{n-1}}\cos(\Omega_{n-1} t)]\rho_{n-1,n-1},\\
\left[\mathbb{R}_e^{ab}\rho\right]_{nn} &= \tfrac{1}{2}[1 - e^{-t/\tau_n}\cos(\Omega_n t)]\rho_{n+1,n+1},\\
\left[\mathbb{R}_g^{ab}\rho\right]_{nn} &= \tfrac{1}{2}[1 + e^{-t/\tau_{n-1}}\cos(\Omega_{n-1} t)]\rho_{nn},
\end{aligned} \tag{37}$$

where we define $\rho_{-1,-1} \equiv 0$ and $e^{-t/\tau_{-1}}\cos(\Omega_{-1}t) \equiv 1$. Since we are interested only in the diagonal elements of ρ, we do not give here the transformations of its nondiagonal elements.

Control samples contain on purpose a small average atom number (typically 0.5, in contrast with 1.3 atoms on average in sensor samples) in order to limit the probability of having two atoms at a time, jeopardizing the field jump correction. However, two atom events have to be taken into account when estimating the field state after an actuator sample detection. In contrast to the case of the dispersive interaction (14), the simultaneous coupling of two resonant atoms to the field can not be represented as a product of two independent one-atom interactions, i.e., $R_{s_1 s_2}^\nu \neq R_{s_1}^\nu R_{s_2}^\nu$ for s_1 and $s_2 \in \{g,e\}$ and $\nu \in \{em,ab\}$. The theoretical evolution of two atoms resonantly coupled to the cavity field and its experimental calibration are given in Appendix C. Based on these results, we get the set of superoperators $\mathbb{R}_\mu^\nu$, with $\mu \in \{ee,eg,gg\}$ [see Eq. (C10)].

We take into account the atom-number Poisson distribution in the actuator samples as we did for sensor samples [see Eq. (14)]. The superoperators $\mathbb{L}_\mu^\nu$ describing the field evolution produced by the resonant interaction with an actuator containing up to two atoms, followed by the ideal detection result μ, are thus given by

$$\begin{aligned}
&\mathbb{L}_\varnothing^\nu = P_\text{a}(0)\mathbb{I}, \quad \mathbb{L}_g^\nu = P_\text{a}(1)\mathbb{R}_g^\nu, \quad \mathbb{L}_e^\nu = P_\text{a}(1)\mathbb{R}_e^\nu,\\
&\mathbb{L}_{gg}^\nu = P_\text{a}(2)\mathbb{R}_{gg}^\nu, \quad \mathbb{L}_{ge}^\nu = 2\,P_\text{a}(2)\mathbb{R}_{ge}^\nu, \quad \mathbb{L}_{ee}^\nu = P_\text{a}(2)\mathbb{R}_{ee}^\nu,
\end{aligned} \tag{38}$$

where $\mathbb{I}$ is the unity superoperator.

The effects of the limited detection efficiency and state resolution of D can be included as for the sensor samples. The detection result μ' of an actuator of type $\nu \in \{em,ab\}$ can be expressed [see also Eq. (17)] as

$$\mathbb{M}_{\mu'}^\nu \rho = \frac{\sum_\mu P_{ac}(\mu'|\mu)\,\mathbb{L}_\mu^\nu \rho}{\text{Tr}\big(\sum_\mu P_{ac}(\mu'|\mu)\,\mathbb{L}_\mu^\nu \rho\big)}. \tag{39}$$

The conditional detection probabilities $P_{ac}(\mu'|\mu)$ are to be taken from Table I, substituting the effective detection errors of the Ramsey interferometer $\eta_{e/g}$ by the pure detection errors $\tilde{\eta}_{e/g}$ of D.

The action of a not-yet-detected actuator on the field's state is described by the superoperator

$$\mathbb{N}^{\nu}\rho = \sum_{\mu} \mathbb{L}^{\nu}_{\mu}\rho. \tag{40}$$

Note that, as mentioned above, a discarded actuator, being off resonant, does not change the field's energy and provides no information on the field since it is always detected in its initial state. Therefore, the superoperators $\mathbb{M}^{ds}_{\mu'}$ and $\mathbb{N}^{ds}$ related to a discarded sample are both unity:

$$\mathbb{M}^{ds}_{\mu'}\rho = \mathbb{N}^{ds}\rho = \rho. \tag{41}$$

C. Quantum state estimation

The state estimation (17) after the detection of a sensor sample can be somewhat simplified. Since ρ is always diagonal, unread sensor measurements do not change it. The state estimation, which thus does not depend on the detection efficiency ε, consequently simplifies to

$$\mathbb{M}^{sn}_{\mu'}\rho = \frac{\sum_{\mu} P_{sn}(\mu'|\mu)\, \mathbb{L}^{sn}_{\mu}\rho}{\mathrm{Tr}\big(\sum_{\mu} P_{sn}(\mu'|\mu)\, \mathbb{L}^{sn}_{\mu}\rho\big)}, \tag{42}$$

where the conditional probabilities $P_{sn}(\mu'|\mu)$ are given in Table I with ε set to 1. Obviously, the state transformation due to a not-yet-detected sensor is unity:

$$\mathbb{N}^{sn}\rho = \rho. \tag{43}$$

Since the distance between two successive samples is smaller than the size of the cavity mirrors, the electric pulse $V_{\rm res}$ applied across C in order to tune an actuator in resonance spoils the phase of a neighboring sensor, which is also located between the mirrors at this time. Therefore, the measurement of a sensor neighboring an actuator does not provide reliable information on the field and we always replace $\mathbb{M}^{sn}_{\mu'}$ by unity in this case.

Using the state transformations for all possible sample types and detection results and taking into account decoherence, we obtain the complete state estimate ρ_k after detection of the kth sample:

$$\rho_k = \prod_{i=k+1}^{k+s} (\mathbb{T}\mathbb{N}^{\nu_i}) \prod_{i=1}^{k} \big(\mathbb{T}\mathbb{M}^{\nu_i}_{\mu'_i}\big)\rho_0. \tag{44}$$

Here, the detection result of the ith sample is $\mu'_i \in \{\varnothing, g, e, gg, ge, ee\}$ and its type is $\nu_i \in \{sn, em, ab, ds\}$. The first k samples have been already detected, while the last s have interacted with C but are still flying towards D.

As already stressed, the field density matrix stays always diagonal in this experiment. The state estimation (44) is performed only with the photon-number distribution requiring thus less computing power than the feedback experiments with coherent injections.

To reduce the calculation time further, we truncate the Hilbert space to the first 9 Fock states for $n_{\rm t} = 1$ to 5 and to the first 10 states for $n_{\rm t} = 6$ to 7. We also approximate the left product in (44) by

$$\prod_{i=k+1}^{k+s} (\mathbb{T}\mathbb{N}^{\nu_i}) \approx (\mathbb{T})^s \prod_{i=k+1}^{k+s} \mathbb{N}^{\nu_i} \tag{45}$$

and precalculate the constant power term $(\mathbb{T})^s$. The validity of (45) has been confirmed by numerical simulations of the experiment.

D. Controller decision

1. Distance

The controller's task is to find the actuator action which minimizes the distance, defined by (23) and (24), of the updated field state to the target $n_{\rm t}$. For the photon-number distribution $p(n)$, this distance can be rewritten as

$$d(n_{\rm t}, p(n)) = \sum_i d_{n_{\rm t}}(i)\, p(i). \tag{46}$$

The values of $d_{n_{\rm t}}(n)$ presented in Fig. 4 were adapted for the coherent feedback and derived from the properties of the displacement operator. They are thus not *a priori* optimal for the atomic actuator feedback.

Emitter and absorber samples are equally efficient for adding or removing a photon in the cavity. This suggests the use of coefficients $d_{n_{\rm t}}(n)$ symmetric around $n_{\rm t}$. Therefore, we choose the distance as

$$d(n_{\rm t}, p(n)) = \sum_i (i - n_{\rm t})^2 p(i) = (\bar{n} - n_{\rm t})^2 + \Delta n^2 \tag{47}$$

with $\bar{n}$ and Δn^2 denoting, respectively, the mean value and the variance of the photon-number distribution. Minimizing this distance thus results in pushing $\bar{n}$ closer to $n_{\rm t}$ and in narrowing $p(n)$. In matrix form, the distance is

$$d(n_{\rm t}, p(n)) = \mathrm{Tr}\big[\mathfrak{D}'_{n_{\rm t}}\rho\big] \tag{48}$$

with a diagonal distance matrix

$$\mathfrak{D}'_{n_{\rm t}} = \sum_i (i - n_{\rm t})^2\, |i\rangle\, \langle i|\,. \tag{49}$$

By numerical Monte Carlo simulations of the experiment (see Appendix B), we have compared the feedback performance based on the distance (47) to that based on several other definitions, such as $d_{n_{\rm t}}(n) = \sqrt{|n - n_{\rm t}|}$, $d_{n_{\rm t}}(n) = |n - n_{\rm t}|$, or $d_{n_{\rm t}}(n) = 1 - \delta_{nn_{\rm t}}$. Note that the latter definition corresponds to the simple maximization of $p(n_{\rm t})$. The best performance, i.e., the shortest convergence time $\tau_{\rm conv}(n_{\rm t})$ and the highest $\overline{p}(n_{\rm t})$, are obtained for the distance defined by (47).

2. Action

For the kth feedback loop, the controller can make decisions on the three samples $k+8$, $k+7$, and $k+6$, provided they are of the control type. The type ν_{k+8} of the $(k+8)$th sample can be set as sensor, emitter, or absorber. The types ν_{k+7} and ν_{k+6} of the two other samples can be either left unchanged or set as discarded, if they were chosen as actuators, or set back to their initial actuator type if they have been set to the discarded type in the previous loop. For all possible sets $\{\nu_{k+8}, \nu_{k+7}, \nu_{k+6}\}$, K estimates the field state after the interaction of C with these three samples (considering of course that the final detection outcomes are yet unknown). The controller computes the distance of all these states to the target

$$
\begin{aligned}
d^{\{\nu_{k+8},\nu_{k+7},\nu_{k+6}\}} &= \mathrm{Tr}\left[\mathfrak{D}'_{n_{\rm t}} \prod_{i=k+6}^{k+8} \left(\mathbb{T}\,\mathbb{N}^{\nu_i}\right)\rho_k\right] \\
&\approx \mathrm{Tr}\left[\mathfrak{D}'_{n_{\rm t}} (\mathbb{T})^3 \prod_{i=k+6}^{k+8} \mathbb{N}^{\nu_i}\,\rho_k\right]. \qquad (50)
\end{aligned}
$$

It then selects the set of three samples' types minimizing the distance.

At the end of the kth loop, K constructs a time sequence of digital pulses and voltages that will control microwave injection into the Ramsey zones R_1 and R_2, and the electric field in C during the next $(k+1)$st loop. The values and timings of these controls are set according to the assigned types of the samples $k+8$, $k+6$, and $k+4$, which will cross the centers of R_1, C, and R_2, respectively, in the next loop. The sequence is then uploaded to the corresponding output boards of the ADwin system and can not be modified anymore. Its output starts with the beginning of the next loop.

E. Experimental settings

1. Average atom number per sample

The average number of atoms per sample $\overline{m}$ is an important parameter in the optimization of the feedback procedure. As already stressed, its setting must be different for sensor and control samples.

For sensor samples, the goal is to get as much information as possible about the cavity field. This points towards the use of larger $\overline{m}$. This option is supported by numerical simulations, which prove, as seen above, that two dispersive atoms interact independently with C, acquiring thus relevant information. However, this independence does not hold for much more than two atoms. There are then additional atom-number-dependent phase shifts of the atomic coherence. Since D can not measure the exact number of atoms in a sample, the Ramsey fringes for high $\overline{m}$s have a reduced contrast and a shifted phase, affecting the quality of the QND measurement. In order to circumvent this problem, we use the highest $\overline{m}$ value, $\overline{m}_{sn} \approx 1.3$, that does not affect the Ramsey fringes recorded when C is in its vacuum state.

For emitter or absorber samples, the experiment is much more sensitive to the atom number. Already, the interaction of two atoms with C is very different from that of a single one and must be treated independently. For more than two actuator atoms, the description of the interaction becomes more cumbersome and more sensitive to the determination of the experimental parameters. The increase of the number of resonant atoms leads also to a less deterministic feedback action since many photons can be emitted or absorbed simultaneously. We avoid these complications by setting $\overline{m}$ to $\overline{m}_{ct} \approx 0.5$. We accordingly only include one- and two-atom sample actions in the state estimation.

2. Phase shift per photon and Ramsey phase

The calibrated phase shift per photon for the atomic feedback experiments is $\phi_0 = 0.252\pi$ (see Appendix A 1). As in Sec. III, it allows us to discriminate up to eight successive photon numbers of the field.

Let us now choose the value of the Ramsey interferometer phase $\phi_{\rm r}$. The atomic actuators lead to modifications of the photon-number distribution more deterministic than those performed by a classical source. An emitter sample can not remove photons from C and an absorber can not add photons to C. Thus, there is no likelihood that, for instance, the emitter action could populate $|n_{\rm t}-2\rangle$ after a jump to $|n_{\rm t}-1\rangle$ from $|n_{\rm t}\rangle$, as was the case in the coherent feedback case. However, K can still overshoot by injecting or subtracting more than one photon, for instance, with a two-atom sample. It is thus reasonable to set $\phi_{\rm r} = \pi/2 - (n_{\rm t}+1/2)\phi_0$, so that the sensor samples are symmetrically sensitive to states around the target $|n_{\rm t}\rangle$.

3. Partition into sensor and control samples

As explained in Sec. IV A1, the feedback sequence is partitioned in alternating series of N_{sn} sensor and N_{ct} control samples. In order to determine the optimal N_{sn} and N_{ct} values, we perform Monte Carlo simulations of the feedback experiment. The two optimization criteria are the average probability of the target photon-number state $\overline{p}(n_{\rm t})$ and the convergence time $\tau_{\rm conv}(n_{\rm t})$, which is required by K for increasing $\overline{p}(n_{\rm t})$ from 0 (initial vacuum field) to a 0.8 threshold value in 63% of simulated trajectories.

Figure 17 shows $\overline{p}(n_{\rm t})$ and $\tau_{\rm conv}(n_{\rm t})$ as a function of N_{sn} and N_{ct} for $n_{\rm t} = 3$. We chose to set the condition $N_{sn} + N_{ct} \leqslant 20$, so that the duration of one complete cycle is much shorter than $T_{\rm c}$. For each pair of values, we use 2000 quantum trajectories of 145-ms duration. The setting $N_{sn} = 0$ corresponds the situation in which the controller K can decide upon the type of each sample. As we see, this algorithm, if the simplest, is less efficient. The controller, aiming to reduce the distance to the target in each loop, applies actuator samples even if the expected distance reduction is very small and the knowledge on the current state is poor. The better approach would be to regularly send sensor samples, which do not change the distance on average, but provide more information on the state, thus reducing its entropy. As seen in Fig. 17, increasing

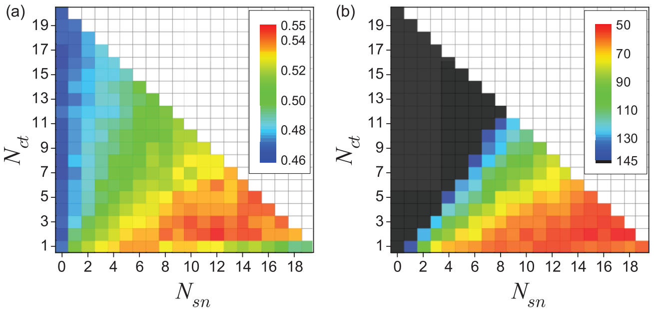

FIG. 17. (Color online) Optimization by Monte Carlo simulations of the sequence partition into N_{sn} sensor and N_{ct} control samples. (a) Average population $\overline{p}(n_{\rm t})$ in the target state $n_{\rm t} = 3$ (2000 trajectories) as a function of N_{sn} and N_{ct} with $N_{sn} + N_{ct} \leqslant 20$. (b) Convergence time $\tau_{\rm conv}(n_{\rm t})$, in ms, for reaching $p(n_{\rm t}) \geqslant 0.8$ in 63% of trajectories used in (a). Dark gray color indicates partitions for which the convergence time is larger than the simulated sequence duration of 145 ms.

N_{sn} indeed improves in general the feedback quality, unless N_{ct} decreases down to 1. In this case, K does not have enough control samples at hand to compensate for the jumps. The region corresponding to $N_{sn} = 10$ to 16 and $N_{ct} = 2$ to 4 features both high $\overline{p}(n_t)$ and short $\tau_{\rm conv}(n_t)$. Experimentally, we have found that the optimal values are $N_{sn} = 12$ and $N_{ct} = 4$.

4. *Resonant interaction times*

Intuitively, the effective atom-cavity interaction time for the resonant emitters or absorbers should be set to achieve an exact π quantum Rabi rotation in the field of $(n_t - 1)$ or $(n_t + 1)$ photons, respectively. These settings lead ideally to the compensation of a quantum jump with a single actuator. The random atom number in a sample and the finite atomic detection efficiency make this simple choice far from optimal. It is impossible to know for sure how many photons have been emitted into the field or absorbed from it by a given sample.

We have therefore to rely also on the information provided by the sensors to determine whether the jump has been corrected or not. This information gathering is not instantaneous and we are thus unable to determine exactly when the target state $|n_t\rangle$ is reached and, hence, when we can stop sending actuators. As a result, there is a large probability for going beyond the required operation and overpumping or overattenuating the field.

One possible solution to avoid these overshoots is to use the "trapping state" condition [26]. When it is fulfilled by the actuator samples, they are unable to alter the target photon-number state. Let us consider first the emitter atoms entering C in state $|e\rangle$. The Rabi frequency in $|n_t\rangle$ is $\Omega_0\sqrt{n_t+1}$. If we set the effective interaction time to $t_e^{2\pi}(n_t) = 2\pi/(\Omega_0\sqrt{n_t+1})$, the emitter undergoes an exact 2π quantum Rabi pulse in the target state. It exits the cavity in $|e\rangle$ and leaves its state unchanged. For initial photon numbers smaller than n_t, however, there is a finite emission probability. Quantum jumps can be corrected, but additional emitter samples do not spoil the restored target state. For absorber samples, the trapping state interaction time is $t_g^{2\pi}(n_t) = 2\pi/(\Omega_0\sqrt{n_t})$. It leads similarly to an unconditional correction of the quantum jumps, independent of the precise number of actuators used.

Unfortunately, experimental imperfections again conspire against this elegant solution. As seen above, the experimental Rabi oscillations have a finite contrast and are damped. Figure 18 shows, as a function of the initial photon number, the resulting photon-exchange probabilities $P_{em}(n)$ [triangles in Fig. 18(a)] and $P_{ab}(n)$ [triangles in Fig. 18(b)] for an emitter and an absorber, respectively, in the trapping state condition for $|n_t = 3\rangle$. Since $P_{em/ab}(n_t)$ are about 20%, instead of zero in the ideal case, the trapping conditions can not ensure the preservation of $|n_t\rangle$. Moreover, the emission or absorption probabilities in $|n_t - 1\rangle$ or $|n_t + 1\rangle$, respectively, are only of the order of 30%–40%. This results in a low efficiency of the actuators, in a slow compensation of the quantum jumps, and thus in a poor overall feedback efficiency.

In order to find the optimal effective interaction times $t_{em}(n_t)$ and $t_{ab}(n_t)$ for emitters and absorbers, we have performed Monte Carlo simulations with different values for these parameters. For each pair $\{t_{em},t_{ab}\}$, we compute the average of $p(n_t)$ over 2000 sequences. Figure 19 presents the results for $n_t = 3$ [Fig. 19(a)] and $n_t = 7$ [Fig. 19(b)]. There is a clear optimum, leading us to choose $t_{em}(n_t) = 0.8t_e^{2\pi}(n_t)$ and $t_{ab}(n_t) = 1.2t_g^{2\pi}(n_t)$. The corresponding experimental emission and absorption probabilities $P_{em}(n)$ and $P_{ab}(n)$ for $n_t = 3$ are shown as squares in the two panels of Fig. 18. The transition probabilities for $|n_t\rangle$ slightly increase with respect to the trapping state conditions. However, the much larger increase of $P_{em}(n_t - 1)$ and $P_{ab}(n_t + 1)$ and the decrease of $P_{em}(n_t + 1)$ and $P_{ab}(n_t - 1)$ make the actuator samples more efficient. This explains qualitatively the improvement of the feedback performance.

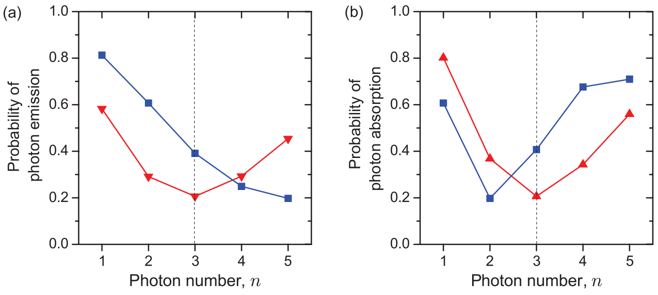

FIG. 18. (Color online) Probability of a photon exchange between photon-number states and actuator atoms. (a) Emission probability of an emitter. Triangles and squares correspond to the effective interaction times $t_e^{2\pi}(n_t)$ and $0.8t_e^{2\pi}(n_t)$, respectively, with $n_t = 3$. (b) Absorption probability of an absorber. Triangles and squares correspond to the interaction times $t_g^{2\pi}(n_t)$ and $1.2t_g^{2\pi}(n_t)$, respectively.

F. Experimental results

1. *Examples of individual trajectories*

Figure 20 shows three feedback sequences with the target photon numbers $n_t = 1$, 4, and 7. The panels, from top to bottom, present, as a function of the total time t, the detection results of the sensor samples, the distance d to the target, the types of actuator samples chosen by K, and, finally, the photon-number distribution $p(n)$ estimated by K. The mean photon number $\overline{n}$ is plotted as a solid black line in the lower panel.

Initially in the vacuum state ($\overline{n} = 0$), the field converges rapidly towards the target [$\overline{n} \approx n_t$ and $p(n_t)$ is close to 1]. When K feels that a quantum jump has occurred, it sends actuator samples to restore n_t. See, for instance, the photon

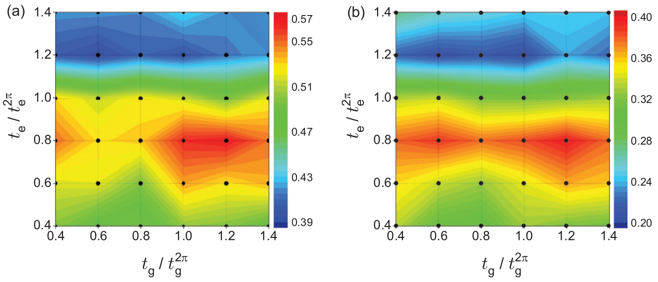

FIG. 19. (Color online) Numerical optimization of the resonant effective interaction times. Average over 2000 sequences of the population in the target state $n_t = 3$ (a) and $n_t = 7$ (b) is calculated for each pair of values t_{em} and t_{ab} marked by black circles. The color (gray) gradient is interpolated to guide the eye.

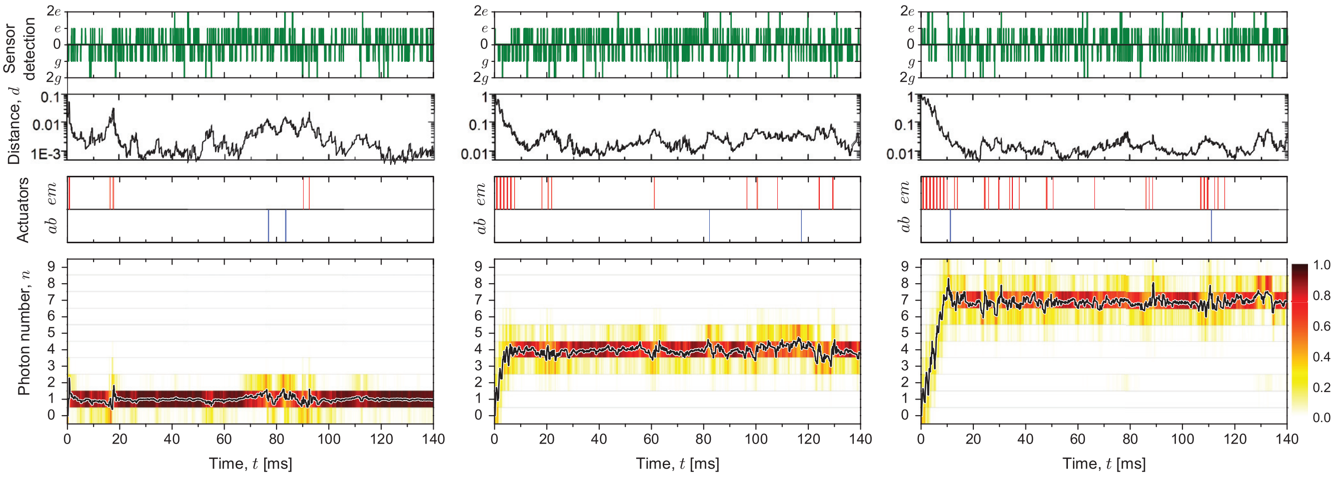

FIG. 20. (Color online) Single sequences of the feedback experiment with $n_{\mathrm{t}} = 1$ (left), $n_{\mathrm{t}} = 4$ (center), and $n_{\mathrm{t}} = 7$ (right). The frames present as a function of the total time t the detected sensor states (upwards bars for e, downwards bars for g), the distance d to n_{t}, the actuators sent by K (red bars for emitters, blue bars for absorbers), and the photon-number distribution $p(n)$ inferred by K [color (grayscale)] together with its mean value $\overline{n}$ (solid black line).

loss around $t = 17$ ms and thermal excitation at $t = 77$ ms for $n_{\mathrm{t}} = 1$, apparent on the change of $\overline{n}$ and on the corresponding increase of d. Sometimes, K sends too many actuators and the jump is overcompensated. It then corrects this error by sending new actuator samples in the opposite state (see, e.g., the overshoots at 10 and 110 ms for $n_{\mathrm{t}} = 7$). It is also conspicuous that the higher the target photon number, the more frequent the jumps and consequently the more actuators sent by K.

2. *Steady-state regime*

The time evolution of the photon-number distribution averaged over 4000 sequences for $n_{\mathrm{t}} = 3$ is shown in Fig. 21. The three curves are the probabilities $\bar{p}(n = n_{\mathrm{t}},t)$ (green, thick line), $\bar{p}(n < n_{\mathrm{t}},t)$ (blue, dotted line), and $\bar{p}(n > n_{\mathrm{t}},t)$ (red, thin line). The steady-state regime, with nearly constant average probabilities, is reached after 20 ms roughly. The residual oscillations, with a period $(N_{sn} + N_{ct})T_{\mathrm{a}}$, are due to the periodic partition of the feedback sequence into N_{sn} sensor and N_{ct} control samples. The only mean-field evolution during the series of sensors is relaxation, leading to a decreasing $\bar{p}(n_{\mathrm{t}},t)$ and to an increasing $\bar{p}(n < n_{\mathrm{t}},t)$. When control samples are sent, K uses the actuators to correct for the field decay, restoring $\bar{p}(n_{\mathrm{t}},t)$ to its maximum value.

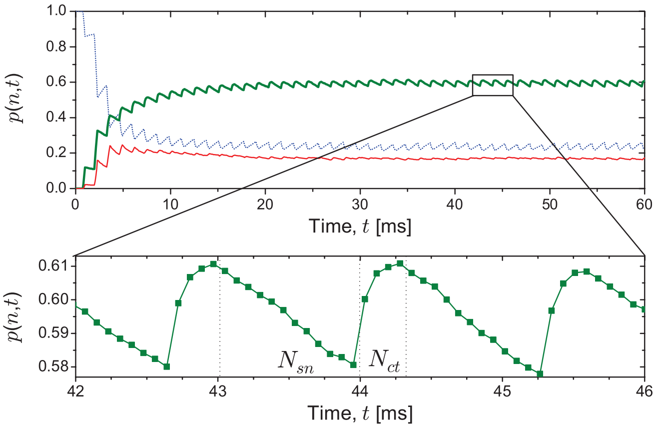

FIG. 21. (Color online) Evolution of the photon-number distribution $\bar{p}(n,t)$ averaged over 4000 feedback sequences with $n_{\mathrm{t}} = 3$. The upper panel shows $\bar{p}(n = n_{\mathrm{t}},t)$ (green, thick curve), $\bar{p}(n < n_{\mathrm{t}},t)$ (blue, dotted curve), and $\bar{p}(n > n_{\mathrm{t}},t)$ (red, thin curve). The lower panel is a zoom into the region highlighted in the upper panel. N_{sn} and N_{ct} indicate the periodic division of the atomic sequence into sensor samples detecting the field decay [reduction of $p(n_{\mathrm{t}})$] and control samples correcting for it [increase of $p(n_{\mathrm{t}})$].

3. *Feedback action versus average photon number*

Since the decision making on the feedback action by K is based on the distance defined by (47), its choice must be correlated with the difference $(\overline{n} - n_{\mathrm{t}})$ between the mean photon number and the target. In Fig. 22, we present the probabilities of the three possible choices for the control samples (emitter, absorber, and sensor) as a function of $(\overline{n} - n_{\mathrm{t}})$. The data are extracted from the analysis of the steady-state regime of 4000 sequences for each target state n_{t} from 1 to 7.

Figure 22 makes it clear that the controller's decision making is similar to a simple rule based only on the comparison of $\overline{n}$ with n_{t}. When $\overline{n} < n_{\mathrm{t}} - 0.4$, K mostly decides to inject a

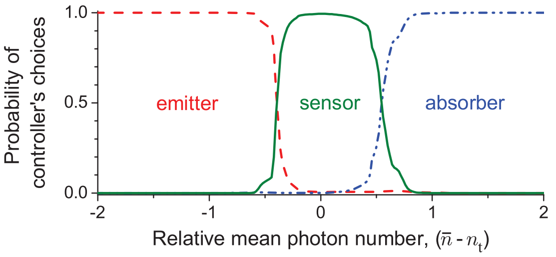

FIG. 22. (Color online) Probabilities of the decision made by K on the control samples (emitter: dashed red line; sensor: solid green line; absorber: dashed-dotted blue line) as a function of $(\overline{n} - n_{\mathrm{t}})$. Data extracted from 4000 realizations of the 140-ms-long experiment for each n_{t}, from 1 to 7.

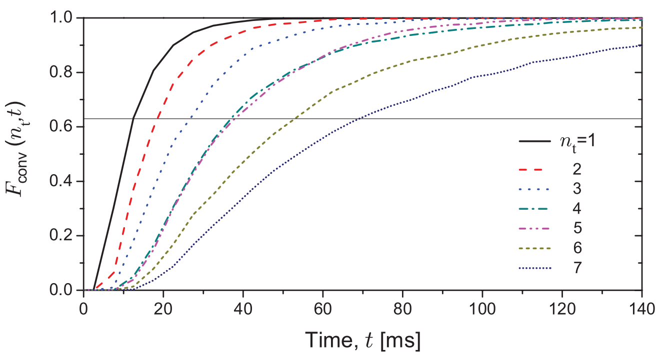

FIG. 23. (Color online) Probability $F_{\mathrm{conv}}(n_{\mathrm{t}},t)$ for $p(n_{\mathrm{t}})$ to reach a 0.8 threshold level for $n_{\mathrm{t}} = 1$ to 7. Each curve is determined from 4000 sequences. The horizontal line shows the 0.63 level defining the convergence time t_{conv}.

photon into C and therefore sets the control samples at hand as emitters. When $\overline{n} > n_{\mathrm{t}} + 0.6$, K sets the control samples as absorbers in order to remove a photon from C. In an interval $n_{\mathrm{t}} - 0.4 < \overline{n} < n_{\mathrm{t}} + 0.6$, with a width $\delta n \approx 1$, the addition or subtraction of a photon does not bring the field any closer to n_{t}. The controller thus decides wisely to use the control samples as sensors. The center of this interval is slightly shifted above n_{t} since K is aware of cavity damping, which alone can get rid of superfluous photons.

The boundaries of the three domains are not sharp, as would be the case with the simple comparison rule. In the intermediate regions, the exact form of $p(n)$ is taken into account, beyond the mere average $\overline{n}$, leading to different possible decisions for the same $\overline{n}$ value. We have compared, using again Monte Carlo simulations, the performance of our complete feedback algorithm with the efficiency of the simpler scheme making decisions based on $\overline{n}$. Our algorithm leads to a slightly higher (by about 2%) fidelity of the target state in the steady state, as well as to a narrower and more symmetric photon-number distribution. This comparison justifies using the more sophisticated algorithm.

4. *Convergence time*

In individual feedback sequences, the fidelity $p(n_{\mathrm{t}})$ can reach relatively high values. We consider, as in Sec. III E4, that the feedback has converged when $p(n_{\mathrm{t}})$ has reached the 0.8 threshold level. The fraction $F_{\mathrm{conv}}(n_{\mathrm{t}},t)$ of sequences which have converged at time t is shown in Fig. 23. For each n_{t} from 1 to 7, we have used 4000 sequences.

At the beginning, all the $F_{\mathrm{conv}}(n_{\mathrm{t}},t)$ curves remain at zero. This period corresponds to the time required to drive the initially empty cavity close to $|n_{\mathrm{t}}\rangle$ by accumulating emitter sample actions. It logically widens when n_{t} increases. At a given time after this initial period, the convergence probability decreases when n_{t} increases. This is obviously due to the more frequent quantum jumps for higher photon numbers.

The convergence time t_{conv}, corresponding to the crossing of the $F_{\mathrm{conv}}(n_{\mathrm{t}},t)$ curve with the 0.63 level (horizontal line in Fig. 23), is given in Table V. For comparison, we also recall in this table the convergence time of the coherent actuator feedback process measured for $n_{\mathrm{t}} = 1$ to 4.

TABLE V. Convergence times t_{conv}, in milliseconds, of the two feedback schemes versus n_{t}.

n_{t}	1	2	3	4	5	6	7
Atomic actuators	12	19	27	37	38	53	69
Microwave source	26	31	49	58			

5. *Photon-number distribution of prepared states*

The independent reconstruction of the photon-number distributions $p_{\mathrm{QND}}(n)$ at the end of the feedback sequence is shown, for $n_{\mathrm{t}} = 1$ to 7, in Fig. 24. For details on the reconstruction method, see Sec. II F. Figure 24(a) presents the theoretical Poisson distributions of the coherent fields with an average photon number $\overline{n} = n_{\mathrm{t}}$. They have the highest possible fidelity with respect to $|n_{\mathrm{t}}\rangle$, which can be obtained with a classical source. The distributions $p_{\mathrm{QND}}(n)$ in the steady-state mode (the feedback sequence stops at a preset 140-ms time) and in the convergence mode (the feedback sequence stops when the 0.8 fidelity threshold has been reached) are shown in Figs. 24(b) and 24(c), respectively. A direct comparison with the results presented in Fig. 10(b) shows that the atomic actuators are more efficient for the stabilization of the quantum Fock states than the coherent injections.

V. CONCLUSION

We have presented in detail the operation of two quantum feedback protocols operating in steady state and stabilizing a photon-number state in a microwave cavity. These experiments are a first demonstration of quantum feedback as an efficient protection mechanism for fragile quantum resources, which could be used, for instance, in quantum information processing experiments. Both protocols use quantum sensors to get QND information on the number of photons in the cavity, realized with atoms interacting dispersively with the cavity mode.

The first protocol uses a classical actuator, a coherent source injecting small amplitudes inside the cavity mode. The experimental implementation is simple, but the feedback is not very efficient to protect high-lying Fock states due to the inadequation between the classical source and the single-photon relaxation-induced quantum jumps which must be corrected. Nevertheless, photon numbers up to 4 are prepared on demand and stabilized with reasonable fidelity, exhibiting the power of the quantum feedback concept.

The second protocol uses quantum actuators, resonant atoms which can add or subtract photons one by one from the cavity mode. Compensation of quantum jumps is much faster, allowing us to stabilize high-lying Fock states up to $n = 7$ with a good fidelity.

In both cases, we have given a detailed description of the experimental procedures and calibrations and of the subtle state estimation that is required to get an efficient stabilization. The relatively slow pace of these microwave-cavity QED experiments and the extremely long cavity lifetimes make it possible to achieve pretty complex calculations during a single feedback loop. Implementing similar procedures in circuit QED [27], for instance, would be very interesting but quite demanding for the control electronics.

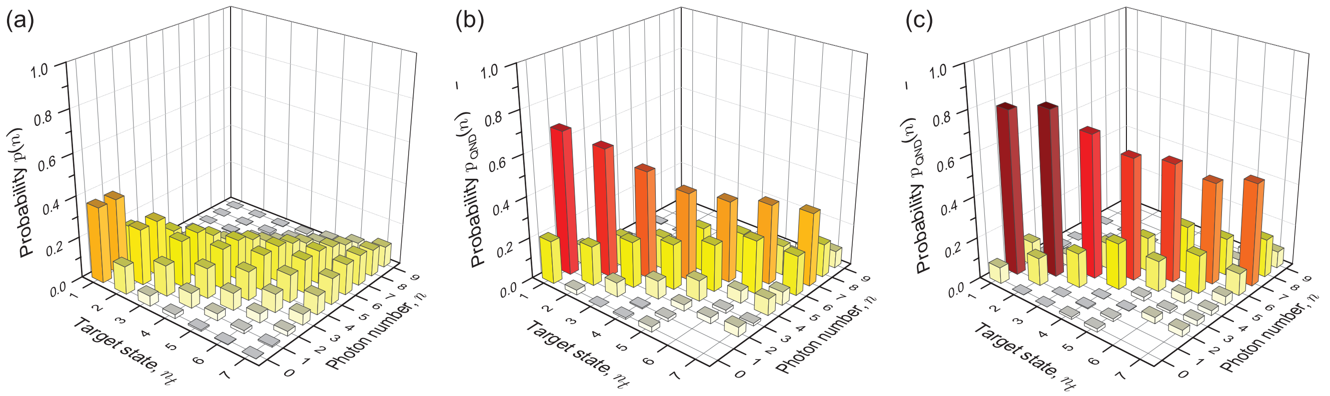

FIG. 24. (Color online) Photon-number distribution prepared by means of the quantum actuator feedback for the target photon numbers n_{t} from 1 to 7. (a) Reference Poisson distribution with n_{t} photons on the average. (b) Photon-number distribution $p_{\mathrm{QND}}(n)$ measured by an independent QND process in the steady-state mode after interrupting the feedback loop at 140 ms. (c) Photon-number distribution $p_{\mathrm{QND}}(n)$ measured in the convergence mode when K estimates that $p(n_{\mathrm{t}}) > 0.8$. For (b) and (c), $p_{\mathrm{QND}}(n)$ is measured from n_0 to $n_0 + 7$, with $n_0 = 0$ for $n_{\mathrm{t}} \leqslant 5$ and $n_0 = 2$ for $n_{\mathrm{t}} > 5$.

The success of these first experiments is quite encouraging for the development of quantum feedback in cavity QED. Some improvements over the present scheme can be envisioned. In the atomic actuator case, for instance, the interaction time of the resonant atoms with the cavity could be used as an additional control parameter to speed up the initial convergence towards the target state. Besides, the choice between sensor and control samples could also be decided upon in real time. So far, the feedback algorithm tries to reduce the distance to the target in each loop, even when the expected improvement is very small. However, from time to time, it could be wiser to acquire more information on the state by sending more sensors before trying to correct it by using actuators. In this case, for instance, the controller's choice for each sample can be made between the reduction of the distance (actuators) and the reduction of the state entropy (sensors).

A quantum feedback scheme could be used to perform extremely efficient QND measurements of the photon number in the cavity. In this scheme, the parameters controlling the interaction of each sensor atom with the cavity field are decided upon dynamically taking into account all information provided by previous atoms. The present method [16], with fixed interaction parameters, requires about 100 atoms to pin down a photon number between 0 and $n_{\max} = 7$. With an ideal adaptative protocol, controlling the atom-cavity interaction time and the Ramsey interferometer phase, we could reduce this number to the minimum required by information theory, $\log_2(n_{\max})$ [28]. Realistic simulations indicate that the practical sample count required could be of the order of 10 only. This achievement would open interesting perspectives for field state reconstruction [29].

Finally, quantum feedback could be used to stabilize against decoherence even more interesting states, for instance, mesoscopic field state superpositions made up of two real coherent components with opposite phases $|\alpha\rangle \pm |-\alpha\rangle$. These states only expand on the even (+ sign) or odd (− sign) photon numbers. Quantum jumps thus correspond to a jump in the photon-number parity. It could be detected by sensor atoms tuned for a $\phi_0 = \pi$ phase shift per photon. Resonant feedback atoms could then be sent to restore the field parity [30].

ACKNOWLEDGMENTS

The authors acknowledge fruitful discussions with P. Rouchon, M. Mirrahimi, and H. Amini and support from European Research Council (DECLIC project), the European Community (AQUTE project) and from the Agence Nationale de la Recherche (QUSCO-INCA project).

APPENDIX A: CALIBRATION OF EXPERIMENTAL PARAMETERS

1. Dispersive atom-field interaction

The phase shift per photon ϕ_0 is an essential parameter for the feedback operation and it must be precisely calibrated each time the atom-cavity detuning is changed. We determine ϕ_0 by the atomic state tomography method described in [20]. We prepare in C a coherent state with about 3–4 photons on the average and send a sequence of 500 dispersive atomic samples with 4 alternating Ramsey phases roughly equal to 0, $\pi/4$, $\pi/2$, and $3\pi/4$. On the average, 0.2 atoms are detected in each sample, leading to about 100 atomic detections per sequence. For all sets of 60 successively detected atoms, we calculate the phase φ_{a} of the e/g superposition at the exit of C correlated to n. Resuming the experiment 4000 times, we get the histogram of the φ_{a} values, with a bin size of 0.02π, shown in Fig. 25(a). The phase origin is here chosen as the phase of the atomic coherence if the cavity interaction is not taken into account. Note that the phase observed for the vacuum state includes the effect of the cavity-induced Lamb shift [31].

In spite of the finite-measurement resolution, well-separated peaks corresponding to the photon numbers n from 0 to 6 are conspicuous. The histogram is fitted by a sum of seven Gaussian peaks with the same 0.27-rad standard deviation width. The position of the peaks relative to the $n = 0$ one, measuring $\phi(n)$, is shown in Fig. 25(b) as a function of the photon number. From a second-order polynomial fit (solid line), we extract $\phi(n)$. Here, $\phi(n) = (0.252 \pm 0.001)\pi(n + 1/2) - (0.001 \pm 0.0004)\pi n^2$. The quadratic term is negligible with respect to the linear one for the values of n considered

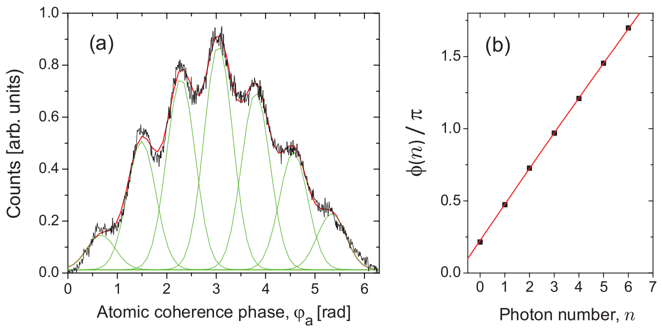

FIG. 25. (Color online) Calibration of the phase shift per photon ϕ_0. (a) Thick black line: histogram of the measured atomic coherence phase φ_a. It is fitted by a sum of seven Gaussian peaks with the same width, corresponding to photon numbers n from zero to six (green thin lines for the individual peaks, red thin line for their sum). (b) Position of the peaks as a function of n (dots) and second-order polynomial fit (line).

in this paper. The linear approximation used in (8) is thus experimentally vindicated and we get $\phi_0 = 0.252\pi$.

2. Detection efficiency

The efficiency ε of the detector D is defined as the ratio between the average number of detected atoms per sample $\overline{m}_{\rm d}$ and the actual average atom number $\overline{m}$: $\varepsilon = \overline{m}_{\rm d}/\overline{m}$. The value of $\overline{m}_{\rm d}$ can be directly measured. In order to obtain $\overline{m}$, we perform an auxiliary experiment. An atomic sample with $\overline{m}_{\rm d} \approx 0.06$ is prepared in $|e\rangle$ and sent through the empty cavity. It interacts resonantly with C, the effective interaction time being tuned for a π quantum Rabi pulse, leaving ideally a photon in C and an atom in $|g\rangle$.

Due to the experimental imperfections in the resonant interaction, we measure a transfer rate from $|e\rangle$ to $|g\rangle$ limited to $\chi = 0.8$. The average number of photons $\overline{n}$ left by this sample in C is thus $\overline{n} = \chi\overline{m}$. For small average atom numbers $\overline{m}$, the probability $P_{\rm a}(>1)$ to have more than one atom per sample is negligible. We have then

$$\overline{m} = P_a(1) = P_{\rm a}(1|1d)P_{\rm a}(1d) + P_{\rm a}(1|0d)P_{\rm a}(0d), \quad \text{(A1)}$$

where $P_a(1)$ is the probability to have one atom in the sample, $P_{\rm a}(1|1d) = 1$ the probability for having one atom provided we have detected one, and $P_{\rm a}(1|0d)$ the probability for having one atom provided none has been detected. We define $P_{\rm a}(1d) = \overline{m}_{\rm d}$ and $P_{\rm a}(0d) = 1 - P_{\rm a}(1d)$ as the probabilities to detect one or zero atom, respectively. We can then write $\overline{m}$ as

$$\overline{m} = \overline{m}_{\rm d} + p(1|0d)/\chi\,(1 - \overline{m}_{\rm d}), \quad \text{(A2)}$$

where $p(1|0d)$ is the probability for the field to contain one photon if no resonant atom has been detected. The detector efficiency is then

$$\varepsilon = \left(1 + \frac{p(1|0d)}{\chi}\frac{1 - \overline{m}_{\rm d}}{\overline{m}_{\rm d}}\right)^{-1}. \quad \text{(A3)}$$

The probability $p(1|0d)$ is measured by sending a sequence of dispersive atomic samples and by recording with them

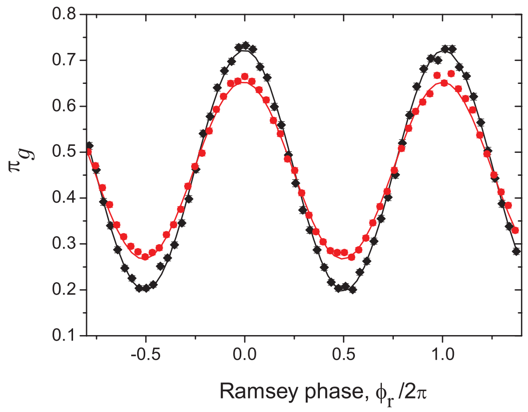

FIG. 26. (Color online) Measurement of the detector efficiency ε. Ramsey fringes $\pi_g(\phi_{\rm r},0)$ in the vacuum field (black with larger contrast) and Ramsey fringes $\pi_g(\phi_{\rm r},0d)$ conditioned on no atom being detected in the resonant sample (red with smaller contrast).

the Ramsey fringes $\pi_g(\phi_{\rm r},0d)$ conditioned on no atom being detected in the resonant sample (Fig. 26). The resulting Ramsey signal can be expressed as the weighted sum of the fringes in the vacuum and one-photon field:

$$\pi_g(\phi_{\rm r},0d) = [1 - p(1|0d)]\,\pi_g(\phi_{\rm r},0) + p(1|0d)\,\pi_g(\phi_{\rm r},1). \quad \text{(A4)}$$

The signal $\pi_g(\phi_{\rm r},0)$ is directly measured with the initial vacuum field in C (see Fig. 26). In order to achieve the largest sensitivity to one injected photon, we adjust for this calibration the phase shift per photon to $\phi_0 \approx \pi$. The one-photon Ramsey fringes in (A4) are in phase opposition with the vacuum ones, i.e., $\pi_g(\phi_{\rm r},0) \approx 1 - \pi_g(\phi_{\rm r},1)$. The fit to $\pi_g(\phi_{\rm r},0d)$ thus yields $p(1|0d)$ and hence ε. With the signals presented here, for instance, we get $p(1|0d) = 0.15$ and $\varepsilon = 0.35$. This value of ε is typical of the coherent feedback measurements. This efficiency deteriorated down to 0.25 for the atomic feedback experiments.

3. Microwave injection

The scheme of the circuit used to control the amplitude and the phase of the microwave injections into C is presented in Fig. 27. The source S generates microwave radiation at 12.8 GHz. It is sent through the first PIN diode switch. The TTL pulse (close level of 0 V and open level of 5 V) controlling this switch defines the duration $t_{\rm S}$ of the injection, and thus the accumulated amplitude. The second PIN diode is used to switch between two paths. One of them includes a variable

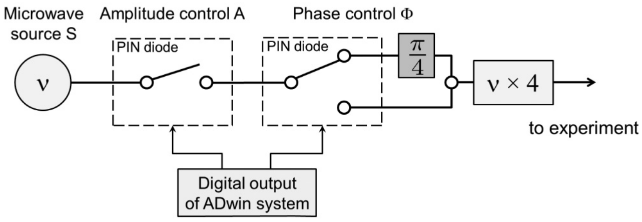

FIG. 27. Control of the injection amplitude and phase.

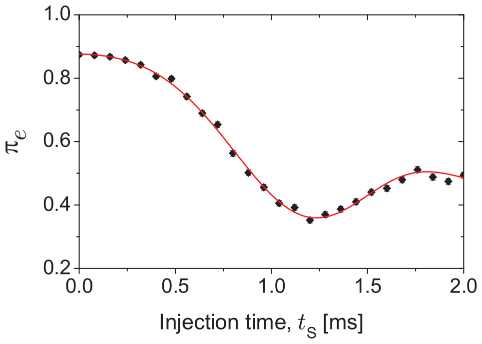

FIG. 28. (Color online) Calibration of the injected amplitude. Dots: probability π_e for detecting the probe atom in $|e\rangle$ as a function of the injection duration t_S. The Ramsey interferometer phase is $\phi_r = -\phi_0/2$. Line: theoretical fit (A5), with τ as the only adjustable parameter.

phase shifter, adjusted to provide a $\pi/4$ phase shift with respect to the other path. The two paths are recombined in a balanced power splitter. Finally, the fourth harmonic of the microwave radiation is generated in a mixer and sent to the experiment. The TTL pulses for the PIN switches are generated by the ADwin system as required to implement the controller's decisions.

The field injection must be precisely calibrated before each experimental run. The modulus $|\alpha|$ of the injected amplitude is a linear function of the injection duration t_S: $|\alpha| = t_S/\tau$, where τ is the time required to inject a one-photon coherent field. We calibrate τ by probing the coherent field produced in C with dispersive atomic sensor samples. The recorded Ramsey signal is then a sum of fringes $\pi_e(\phi_r,n)$ corresponding to different photon numbers n, weighted by the Poisson distribution of n. We choose for this experiment $\phi_r = -\phi_0/2$ [maximum of $\pi_e(\phi_r,0)$], with $\phi_0 \simeq \pi/4$, and measure π_e as a function of t_S. The data are fitted with the analytic fringe summation given by

$$\pi_e(t_S) = \pi_o + \frac{c}{2}\exp\left\{-\left(\frac{t_S}{\tau}\right)^2(1-\cos\phi_0)\right\} \times \cos\left\{\left(\frac{t_S}{\tau}\right)^2\sin\phi_0\right\}. \tag{A5}$$

The result of the fit with the only free parameter $\tau = 633 \pm 4\ \mu$s is shown as a solid line in Fig. 28. The injection time required to reach the maximum feedback amplitude $\alpha_{\max} = 0.1$ is thus 63 μs, shorter than the time interval T_a between atomic samples. The injection calibration is independently performed for the two injection phases realized through two different microwave paths.

For a proper setting of the phase shifter to $\Phi = \pi/4$, we successively inject into the initially empty cavity two microwave pulses of the same amplitude modulus, sent through the two microwave paths. If Φ is set to $\pi/4$, the relative phase of the two pulses after frequency multiplication is π. The final field in C is thus minimal (ideally, it is the vacuum if the cavity decay and the phase noise between the two injections are negligible). We thus adjust Φ by minimizing the residual cavity field, probed by a sequence of dispersive sensor atoms.

APPENDIX B: MONTE CARLO SIMULATIONS

Quantum Monte Carlo simulations [4] have been extensively used in order to test the performance of the quantum feedback and to optimize the experimental parameters. In each feedback loop, we simulate the decoherence of the cavity field, its interaction with the probabilistic atomic samples, and the result of the realistic imperfect atomic detection, which is then used by the controller K to decide upon the feedback action.

The main simulation steps are thus the following. For each sample, at the beginning of each loop, we first randomly choose a number of prepared atoms m by using the Poisson probability distribution (1) with the experimentally determined average atom number $\overline{m}$. The initial state of each atom and its interaction with the field is determined by the sample type (sensor for the coherent injection feedback experiment and sensor, emitter, or absorber for the quantum actuator feedback case). The type is either preset by the original sample sequence or has already been modified by the controller in the previous loops (quantum actuator feedback only).

Knowing the field state at the end of the previous loop, we simulate the result of the virtual ideal detection of the atomic state and then project the field state accordingly. Next, we simulate the result of the real atom detection by using the measured efficiency (ε) and errors ($\tilde{\eta}_{g/e}$ or $\eta_{g/e}$ depending on the feedback scheme) of our real detector D.

This result is then fed in K, which estimates the field's quantum state (Secs. III C or IV C) and which chooses the optimal feedback action (Secs. III D or IV D). In the coherent injection feedback, the displacement operator (19) with the optimal coherent field amplitude α is then applied. Finally, we include the decoherence process during the loop duration T_a by randomly inducing the loss or gain of a photon in the field. The probabilities of these events are given by the jump operators (5) and (6).

APPENDIX C: TWO-ATOM RABI OSCILLATIONS

1. Theoretical description

The Jaynes-Cummings Hamiltonian of the system of $\mathcal{N}$-independent two-level atoms simultaneously and identically coupled to the cavity field reads as [4]

$$H = \hbar\omega_a J_z + \hbar\omega_c\left(a^\dagger a + \frac{1}{2}\right) + \frac{\hbar\Omega_0}{2}(J_+ a + J_- a^\dagger). \tag{C1}$$

The many-atom operators J_z and $J_\pm$ are given by

$$J_z = \frac{1}{2}\sum_j \sigma_{z,j}, \tag{C2}$$

$$J_\pm = \sum_j \sigma_{\pm,j}, \tag{C3}$$

where $\sigma_{z,j}$, $\sigma_{+,j}$, and $\sigma_{-,j}$ are the z component of the Pauli matrices and the atomic raising and lowering operators, respectively, associated to jth atom, viewed as a spin $\frac{1}{2}$. In the resonant case, only considered in the following, the atomic frequency ω_a and the cavity frequency ω_c in (C1) are set to be equal.

The Hamiltonian (C1) conserves the total angular momentum of the $\mathcal{N}$ atoms. In the case of two atoms only, the allowed atomic states constitute a spin-triplet manifold with

$M_J = 0, \pm 1$. The bare states

$$\begin{aligned} |M_J^1\rangle &\equiv |ee,n-1\rangle, \\ |M_J^0\rangle &\equiv |(eg+ge)/\sqrt{2},n\rangle, \\ |M_J^{-1}\rangle &\equiv |gg,n+1\rangle \end{aligned} \tag{C4}$$

with photon number $n \geqslant 1$ constitute a closed subspace of the Hilbert space. In this subspace, the reduced Hamiltonian can be expressed in the matrix form as

$$H_n = \hbar \begin{pmatrix} \omega_c\left(n+\frac{1}{2}\right) & \sqrt{n/2}\,\Omega_0 & 0 \\ \sqrt{n/2}\,\Omega_0 & \omega_c\left(n+\frac{1}{2}\right) & \sqrt{(n+1)/2}\,\Omega_0 \\ 0 & \sqrt{(n+1)/2}\,\Omega_0 & \omega_c\left(n+\frac{1}{2}\right) \end{pmatrix}. \tag{C5}$$

Its eigenenergies are

$$\xi_0 = 0, \quad \pm\hbar\xi_n = \pm\hbar\frac{\Omega_0}{2}\sqrt{2(2n+1)}, \tag{C6}$$

where, without loss of generality, a common term $\hbar\omega_c(n+1/2)$ has been subtracted by redefining the energy origin. The corresponding eigenstates are

$$\begin{aligned} |\psi_0\rangle &= \frac{1}{\sqrt{2n+1}}\left(\sqrt{n+1}\,|M_J^1\rangle - \sqrt{n}\,|M_J^{-1}\rangle\right), \\ |\psi_\pm\rangle &= \frac{1}{\sqrt{2(2n+1)}}\Big(\pm\sqrt{n}\,|M_J^1\rangle + \sqrt{2n+1}\,|M_J^0\rangle \\ &\quad \pm\sqrt{n+1}\,|M_J^{-1}\rangle\Big). \end{aligned} \tag{C7}$$

The bare states $|M_J^1\rangle$ and $|M_J^{-1}\rangle$, which correspond to two emitter and two absorber atoms, respectively, can then be expanded over these eigenstates bases:

$$\begin{aligned} |M_J^1\rangle &= \frac{1}{\sqrt{2n+1}}\left(\sqrt{\frac{n}{2}}(|\psi_+\rangle - |\psi_-\rangle) + \sqrt{n+1}\,|\psi_0\rangle\right), \\ |M_J^{-1}\rangle &= \frac{1}{\sqrt{2n+1}}\left(\sqrt{\frac{n+1}{2}}(|\psi_+\rangle - |\psi_-\rangle) - \sqrt{n}\,|\psi_0\rangle\right). \end{aligned}$$

After a time interval t, they evolve into

$$\begin{aligned} |M_J^1\rangle \xrightarrow{t} &\left[1 + \frac{n}{2n+1}[\cos(\xi_n t) - 1]\right]|M_J^1\rangle \\ &- i\sqrt{\frac{n}{2n+1}}\sin(\xi_n t)\,|M_J^0\rangle \\ &+ \frac{\sqrt{n(n+1)}}{2n+1}[\cos(\xi_n t) - 1]\,|M_J^{-1}\rangle, \end{aligned} \tag{C8}$$

$$\begin{aligned} |M_J^{-1}\rangle \xrightarrow{t} &\frac{\sqrt{n(n+1)}}{2n+1}[\cos(\xi_n t) - 1]\,|M_J^1\rangle \\ &- i\sqrt{\frac{n+1}{2n+1}}\sin(\xi_n t)\,|M_J^0\rangle \\ &+ \left[1 + \frac{n+1}{2n+1}[\cos(\xi_n t) - 1]\right]|M_J^{-1}\rangle. \end{aligned} \tag{C9}$$

The three possible results of an ideal atomic detection $\{ee,eg,gg\}$ correspond to a projection into the states $|M_J^1\rangle$, $|M_J^0\rangle$, and $|M_J^{-1}\rangle$, respectively.

The two-atom superoperators $\mathbb{R}_\mu^\nu$, analogous to (37), for the time being in an ideal situation are

$$\begin{aligned} [\mathbb{R}_{ee}^{em}\rho]_{nn} &= \left(1 + \frac{n+1}{2n+3}[\cos(\xi_{n+1}t) - 1]\right)^2 \rho_{nn}, \\ [\mathbb{R}_{eg}^{em}\rho]_{nn} &= \left(\frac{n}{2n+1}\sin^2(\xi_n t)\right)\rho_{n-1,n-1}, \\ [\mathbb{R}_{gg}^{em}\rho]_{nn} &= \left(\frac{n(n-1)}{2n-1}[\cos(\xi_{n-1}t) - 1]^2\right)\rho_{n-2,n-2}, \\ [\mathbb{R}_{ee}^{ab}\rho]_{nn} &= \left(\frac{(n+1)(n+2)}{(2n+3)^2}[\cos(\xi_{n+1}t) - 1]^2\right)\rho_{n+2,n+2}, \\ [\mathbb{R}_{eg}^{ab}\rho]_{nn} &= \left(\frac{n+1}{2n+1}\sin^2(\xi_n t)\right)\rho_{n+1,n+1}, \\ [\mathbb{R}_{gg}^{ab}\rho]_{nn} &= \left(1 + \frac{n}{2n-1}[\cos(\xi_{n-1}t) - 1]\right)^2 \rho_{n,n} \end{aligned} \tag{C10}$$

with ξ_{-1} being understood as zero.

2. Experimental imperfections

Figure 29 shows the measured Rabi oscillations of two atoms simultaneously coupled to the cavity mode. The average detected atom number per sample is set to 0.06. All atoms are

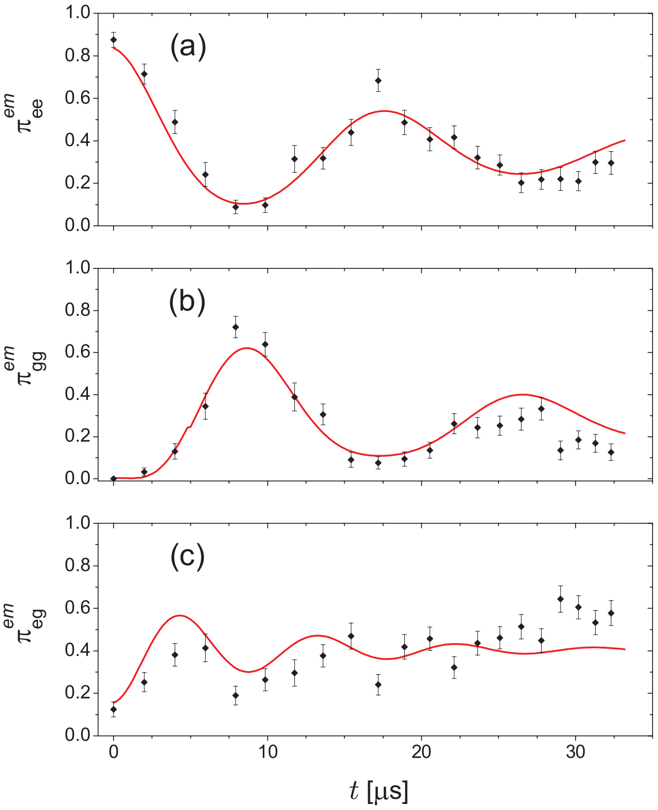

FIG. 29. (Color online) Rabi oscillations of two atoms both prepared in state $|e\rangle$ and simultaneously coupled to the cavity mode. The atoms are detected both in $|e\rangle$ (a), both in $|g\rangle$ (b), or one in $|e\rangle$ and the other in $|g\rangle$ (c). Solid red lines are theoretical fits with the phenomenological exponential damping.

initially prepared in state $|e\rangle$ and the two-atom detection events are post-selected. Figures 29(a), 29(b), and 29(c) present the probabilities of the three possible detection results for two atoms, namely, ee, gg, and eg, respectively. By setting $n = 1$ in (C8), we obtain their theoretical expressions

$$\begin{aligned}\pi^{em}_{ee}(t) &= \frac{1}{2} + \frac{1}{18}\cos(\sqrt{6}\Omega_0 t) + \frac{4}{9}\cos\left(\frac{\sqrt{6}\Omega_0 t}{2}\right),\\ \pi^{em}_{gg}(t) &= \frac{1}{3} + \frac{1}{9}\cos(\sqrt{6}\Omega_0 t) - \frac{4}{9}\cos\left(\frac{\sqrt{6}\Omega_0 t}{2}\right),\\ \pi^{em}_{eg}(t) &= \frac{1}{6} - \frac{1}{6}\cos(\sqrt{6}\Omega_0 t). \end{aligned} \tag{C11}$$

As in the one-atom case, we introduce now a phenomenological exponential damping, $\exp(-t/\tau_n^{(2)})$, for all oscillating terms in (C10) with the damping times

$$\tau_n^{(2)} = \tau_0^{(2)}/\sqrt{2(2n+1)}, \tag{C12}$$

which are also inversely proportional to the many-photon Rabi frequency, similarly to (34). To include this damping, we multiply the terms oscillating at frequencies $\sqrt{6}\Omega_0$ and $\sqrt{6}\Omega_0/2$ by $\exp(-\sqrt{6}t/\tau_0^{(2)})$ and $\exp(-\sqrt{6}t/2\tau_0^{(2)})$, respectively.

The solid lines in Fig. 29 present the fits of the experimental data with the damped oscillations (C11). The fit parameters are the offsets of the $\pi^{em}_\mu(t)$ functions, the amplitudes of all oscillating terms, and the damping time $\tau_0^{(2)}$. We have also used the fact that the $\pi^{em}_\mu(t)$ sum up to 1 and we have set $\Omega_0/2\pi = 46$ kHz. The obtained values of $\tau_0^{(2)} = 35$ μs and of all offsets and contrasts are then used to construct the realistic resonant two-atom superoperators.

[1] V. B. Braginsky and F. Y. Khalili, *Quantum Measurement* (Cambridge University Press, Cambridge, UK, 1999).

[2] H. M. Wiseman and G. J. Milburn, *Quantum Measurement and Control* (Cambridge University Press, Cambridge, UK, 2009).

[3] D. Leibfried, R. Blatt, C. Monroe, and D. Wineland, Rev. Mod. Phys. **75**, 281 (2003).

[4] S. Haroche and J. M. Raimond, *Exploring the Quantum: Atoms, Cavities and Photons* (Oxford University Press, Oxford, UK, 2006).

[5] B. D'Urso, B. Odom, and G. Gabrielse, Phys. Rev. Lett. **90**, 043001 (2003).

[6] P. Bushev, D. Rotter, A. Wilson, F. Dubin, C. Becher, J. Eschner, R. Blatt, V. Steixner, P. Rabl, and P. Zoller, Phys. Rev. Lett. **96**, 043003 (2006).

[7] M. Koch, C. Sames, A. Kubanek, M. Apel, M. Balbach, A. Ourjoumtsev, P. W. H. Pinkse, and G. Rempe, Phys. Rev. Lett. **105**, 173003 (2010).

[8] S. Brakhane, W. Alt, T. Kampschulte, M. Martinez-Dorantes, R. Reimann, S. Yoon, A. Widera, and D. Meschede, Phys. Rev. Lett. **109**, 173601 (2012).

[9] R. J. Nelson, Y. Weinstein, D. Cory, and S. Lloyd, Phys. Rev. Lett. **85**, 3045 (2000).

[10] W. P. Smith, J. E. Reiner, L. A. Orozco, S. Kuhr, and H. M. Wiseman, Phys. Rev. Lett. **89**, 133601 (2002).

[11] R. L. Cook, P. J. Martin, and J. M. Geremia, Nature (London) **446**, 774 (2007).

[12] G. G. Gillett, R. B. Dalton, B. P. Lanyon, M. P. Almeida, M. Barbieri, G. J. Pryde, J. L. O'Brien, K. J. Resch, S. D. Bartlett, and A. G. White, Phys. Rev. Lett. **104**, 080503 (2010).

[13] R. Vijay, C. Macklin, D. H. Slichter, S. J. Weber, K. W. Murch, R. Naik, A. N. Korotkov, and I. Siddiqi, Nature (London) **490**, 77 (2012).

[14] C. Sayrin, I. Dotsenko, X. Zhou, B. Peaudecerf, T. Rybarczyk, S. Gleyzes, P. Rouchon, M. Mirrahimi, H. Amini, M. Brune, J. M. Raimond, and S. Haroche, Nature (London) **477**, 73 (2011).

[15] X. Zhou, I. Dotsenko, B. Peaudecerf, T. Rybarczyk, C. Sayrin, S. Gleyzes, J. M. Raimond, M. Brune, and S. Haroche, Phys. Rev. Lett. **108**, 243602 (2012).

[16] C. Guerlin, J. Bernu, S. Deléglise, C. Sayrin, S. Gleyzes, S. Kuhr, M. Brune, J. M. Raimond, and S. Haroche, Nature (London) **448**, 889 (2007).

[17] S. Kuhr, S. Gleyzes, C. Guerlin, J. Bernu, U. B. Hoff, S. Deléglise, S. Osnaghi, M. Brune, J. M. Raimond, S. Haroche, E. Jacques, P. Bosland, and B. Visentin, Appl. Phys. Lett. **90**, 164101 (2007).

[18] P. Nussenzveig, F. Bernardot, M. Brune, J. Hare, J. M. Raimond, S. Haroche, and W. Gawlik, Phys. Rev. A **48**, 3991 (1993).

[19] D. F. Walls and G. J. Milburn, *Quantum Optics* (Springer, Berlin, 1994).

[20] M. Brune, J. Bernu, C. Guerlin, S. Deléglise, C. Sayrin, S. Gleyzes, S. Kuhr, I. Dotsenko, J. M. Raimond, and S. Haroche, Phys. Rev. Lett. **101**, 240402 (2008).

[21] C. Sayrin, I. Dotsenko, S. Gleyzes, M. Brune, J. M. Raimond, and S. Haroche, New J. Phys. **14**, 115007 (2012).

[22] A. I. Lvovsky, H. Hansen, T. Aichele, O. Benson, J. Mlynek, and S. Schiller, Phys. Rev. Lett. **87**, 050402 (2001).

[23] I. Dotsenko, M. Mirrahimi, M. Brune, S. Haroche, J. M. Raimond, and P. Rouchon, Phys. Rev. A **80**, 013805 (2009).

[24] H. Khalil, *Nonlinear Systems* (Prentice Hall, Englewood Cliffs, NJ, 2001).

[25] H. Amini, A. Somaraju, I. Dotsenko, C. Sayrin, M. Mirrahimi, and P. Rouchon, IEEE Trans. Automatic Control (to be published).

[26] M. Weidinger, B. T. H. Varcoe, R. Heerlein, and H. Walther, Phys. Rev. Lett. **82**, 3795 (1999).

[27] M. D. Reed, L. DiCarlo, S. E. Nigg, L. Sun, L. Frunzio, S. M. Girvin, and R. J. Schoelkopf, Nature (London) **482**, 382 (2012).

[28] S. Haroche, M. Brune, and J. M. Raimond, J. Phys. II **2**, 659 (1992).

[29] S. Deléglise, I. Dotsenko, C. Sayrin, J. Bernu, M. Brune, J. M. Raimond, and S. Haroche, Nature (London) **455**, 510 (2008).

[30] D. Vitali, S. Zippilli, P. Tombesi, and J. M. Raimond, J. Mod. Opt. **51**, 799 (2004).

[31] M. Brune, P. Nussenzveig, F. Schmidt-Kaler, F. Bernardot, A. Maali, J. M. Raimond, and S. Haroche, Phys. Rev. Lett. **72**, 3339 (1994).